Consistent and conservative scheme for incompressible two-phase flows using the conservative Allen-Cahn model

Ziyang Huang*1, Guang Lin^{†1,2}, and Arezoo M. Ardekani^{‡1}

School of Mechanical Engineering, Purdue University, West Lafayette, IN 47907, USA
 Department of Mathematics, Purdue University, West Lafayette, IN 47907, USA

Abstract

In the present work, we consider the conservative Allen-Cahn model and applied it to two-phase flows in a consistent and conservative manner. The consistent formulation is proposed, where the conservative Allen-Cahn equation is reformulated in a conservative form using an auxiliary variable. As a result, the consistency analysis is performed and the resulting two-phase model honors the consistency of reduction, the consistency of mass conservation and the consistency of mass and momentum transport, which are important to reproduce the physical momentum and kinetic energy transport, to achieve mass and momentum conservation, and to satisfy the energy law of the two-phase system. A consistent and conservative scheme is developed, and its properties are carefully analyzed and validated. In order to honor the maximum principle of the conservative Allen-Cahn model, we proposed a boundedness mapping algorithm, which preserves the properties of consistency and conservation of the scheme. The applications of the consistent formulation and the proposed scheme to realistic two-phase flows show that they are accurate, robust and effective for complicated two-phase problems. The applicability of the consistent formulation and consistency analysis to multiphase flows and to the improved Cahn-Hilliard model is discussed.

Keywords: The conservative Allen-Cahn model; Phase-Field; Consistent scheme; Conservative scheme; Two-phase flow; large density ratio

1 Introduction

Two-phase flows are ubiquitous and have wide-spread applications. There are many challenges in studying this kind of problem, for example, the strong interactions between the fluid phases, the motion and deformation of the interfaces, and the appearance of topological changes. As a result, numerical simulation becomes a powerful tool to study this kind of problem. There have been many successful numerical models developed and greatly improved in the recent decade. To locate the interface, one can use the Front-Tracking method [67, 66], the Volume-of-Fluid (VOF) method [20, 55, 50, 49], the Level-Set method [48, 63, 56, 18], the conservative Level-Set method [46, 47, 11], the "THINC" method [69, 25, 70, 52], or their coupling. To model the surface tension at the moving interface, one can use, e.g., the continuous surface force (CSF) [6] or the ghost fluid method (GFM) [16, 36]. The balanced-force algorithm is developed in [17, 51] to improve the numerical force balance between the surface tension and the pressure jump. All these methods are categorized in the sharp-interface model [37], where the interface thickness is assumed to be zero. However, some artificial interfacial regions may be introduced in the discretization to improve numerical stability.

Another popular model for two-phase flows is the Phase-Field (diffuse interface) model [4], where the interface thickness is assumed to be small but finite. The interface thickness is maintained by the thermodynamic compression and diffusion inside the interfacial region. In the Phase-Field model of two-phase flows,

^{*}Email: huan1020@purdue.edu

[†]Email: guanglin@purdue.edu; Corresponding author

[‡]Email: ardekani@purdue.edu; Corresponding author

most attention has been paid to the Cahn-Hilliard model [8], due to its property of global mass conservation, which is physically essential in two-phase flows. Many theoretical or numerical studies have been performed on the two-phase flow model using the Cahn-Hilliard equation, including the asymptotic analysis, e.g., in [42, 1], scaling analysis, e.g., in [26, 75], consistency analysis [22], numerical scheme development, e.g., in [26, 13, 15, 41, 58, 22]. This two-phase model has been extensively applied to study various two-phase problems, e.g., the jet pinching-off and drop formation [72], two-phase complex fluids[73], two-phase Newtonian and viscoelastic fluids[74], Nematic Liquid Crystals[80], two-phase ferrofluid flows [45], and moving contact lines [27, 53, 59]. Some recent work has extended the two-phase flow model to three- or multi-phase flows e.g., in [5, 33, 14].

In the present work, we consider the so-called conservative Allen-Cahn model. It is another Phase-Field model that is plausible for two-phase flows. The original Allen-Cahn model [3] does not conserve mass. To resolve this issue, a Lagrange multiplier is added to enforce the conservation constraint, and the resulting model is called the conservative Allen-Cahn model. The analysis of this model is available, e.g., in [10], and it has been applied to two-phase flows, see a comprehensive review by Shen [57]. A more recent model of this kind is proposed by Brassel and Bretin [7], where a weight function is assigned ahead of the Lagrange multiplier so that the Lagrange multiplier is only effective in the interfacial region. They show that this model not only conserves the global mass exactly but also conserves the mass enclosed by a specific contour, e.g., the zero contour in the present work, at the order of η^2 , where η is the thickness of interface. This is better than the previous conservative Allen-Cahn model without the weight, which conserves the mass enclosed by the zero contour at the order of η . This property is validated in their numerical experiments. A comparison study among the conservative Allen-Cahn models and the Cahn-Hilliard models in [38] also shows that the conservative Allen-Cahn model with a weight outperforms in conserving the mass enclosed by the zero contour. If the zero contour is understood as the interface between the fluid phases, it is desirable to conserve the mass enclosed by the interface. Thus, the conservative Allen-Cahn model in [7] is plausible for two-phase flow modeling. Jeong and Kim [29], and Joshi and Jaiman [32, 31] have coupled the conservative Allen-Cahn equation with the Navier-Stokes equation to model the incompressible two-phase flows, while the consistency conditions, the momentum conservation, and the energy law of the two-phase system were not considered in their models or numerical implementations.

As it is shown in our previous work [22], it is important to satisfy the consistency of reduction, the consistency of mass conservation, and the consistency of mass and momentum transport when applying a Phase-Field model to two-phase flows. Otherwise, the physical transport of the momentum and kinetic energy will be destroyed and the energy law of the two-phase system is violated even in the continuous level, and in the discrete level, unphysical interface deformation and velocity fluctuations are introduced. The challenge of applying the consistency analysis on the conservative Allen-Cahn equation is that the conservation constraint is enforced by a Lagrange multiplier in that equation. As a result, the conservative Allen-Cahn equation has a form of convection-diffusion-reaction equation, and is not in a conservative form, although it satisfies the conservation constraint. To resolve this issue, the consistent formulation is proposed, where we introduce an auxiliary variable whose governing equation is a Poisson equation. We show that the Poisson equation is compatible with its boundary condition and, as a result, it is solvable. After including the auxiliary variable, the conservative Allen-Cahn equation, whose original form is a convection-diffusion-reaction equation, is reformulated in a conservative form and the consistency analysis can be directly applied. Consequently, the consistent two-phase model using the conservative Allen-Cahn equation is developed, which honors the mass conservation, momentum conservation, and energy law. A consistent and conservative scheme is developed to solve the two-phase model and our numerical results show that the proposed model and scheme produce physical results for complicated two-phase problems. To the best of the authors' knowledge, this is the first work that applied the conservative Allen-Cahn model to two-phase flows in a consistent and conservative manner in both the continuous and discrete levels.

The rest of the paper is presented as follows. In Section 2, the conservative Allen-Cahn equation is first introduced, followed by the consistent formulation and analysis. In Section 3, the numerical scheme to solve the two-phase model is described, followed by the analyses of the properties of the scheme. In Section 4, the properties of the model and scheme are first validated, followed by applications of the proposed model and scheme to realistic two-phase flows. In Section 5, we discuss the possible application of the consistent formulation and the proposed scheme to multiphase problems and to the improved Cahn-Hilliard model, followed by an alternative scheme that preserves the maximum principle and the conservation constraint. In

Section 6, we conclude our present work and comment on interesting and valuable future directions.

2 Governing equations

In this section, we summarize the governing equations for two-phase flows using the conservative Allen-Cahn model. We first introduce the conservative Allen-Cahn equation, the momentum equation, and the consistency conditions. Then, the consistent formulation is proposed, where the method to reformulate the conservative Allen-Cahn equation, whose original form is a convection-diffusion-reaction equation, into a conservative form is introduced, along with the analyses of the complete two-phase model on satisfying the consistency conditions.

2.1 The conservative Allen-Cahn equation

The conservative Allen-Cahn equation for two-phase incompressible flows considered in the present work has a form

$$\frac{\partial \phi}{\partial t} + \nabla \cdot (\mathbf{u}\phi) = M\lambda \nabla^2 \phi - \frac{M\lambda}{\eta^2} g'(\phi) + W_q(\phi)q(t), \tag{1}$$

where ϕ is the order parameter of the Phase-Field equation, \mathbf{u} is the velocity, M is the mobility, λ is the mixing energy density, $g(\phi)$ is the double-well potential function and $g'(\phi)$ is its derivative with respect to ϕ , $W_q(\phi)$ is the weight function of q, and q is the Lagrange multiplier, only depending on time t, to enforce the conservation constraint.

Specifically, the incompressibility requires that the velocity is divergence-free, i.e.,

$$\nabla \cdot \mathbf{u} = 0. \tag{2}$$

We consider the double-well potential function to be

$$g(\phi) = \frac{1}{4}(1 - \phi^2)^2,\tag{3}$$

and correspondingly the mixing energy density is

$$\lambda = \frac{3}{2\sqrt{2}}\sigma\eta,\tag{4}$$

where σ is the surface tension between the two fluid phases. From the conservation constraint, i.e., $\frac{d}{dt} \int_{\Omega} \phi d\Omega = 0$, along with the homogeneous Neumann boundary condition for ϕ , i.e., $\mathbf{n} \cdot \nabla \phi = 0$, and with the free-slip boundary condition for \mathbf{u} , i.e., $\mathbf{n} \cdot \mathbf{u} = 0$, where \mathbf{n} is the outward normal at the domain boundary, the Lagrange multiplier q(t) is derived as

$$q(t) = \frac{\int_{\Omega} \frac{M\lambda}{\eta^2} g'(\phi) d\Omega}{\int_{\Omega} W_q(\phi) d\Omega}.$$
 (5)

We majorly consider the weight function $W_q(\phi)$ to be $2\sqrt{g(\phi)}$, which is proposed by Brassel and Bretin [7], i.e.,

$$W_q(\phi) = 1 - \phi^2,\tag{6}$$

although any other choice of $W_q(\phi)$ is acceptable in the present work. As a result, the Lagrange multiplier q(t) is only effective in the interfacial region, i.e., $-1 < \phi < 1$, while it has no influence on the bulk region, i.e., $\phi = \pm 1$. A simpler choice of the weight function is to let it be homogeneous, i.e., $W_q(\phi) \equiv 1$. The analysis of the conservative Allen-Cahn equation with $W_q(\phi) \equiv 1$ without hydrodynamics can be found, e.g., in [10] and this model has been applied to two-phase flows, see the comprehensive review by Shen [57]. As shown in [7], the benefit of using Eq.(6) is that not only the conservation constraint, i.e., $\frac{d}{dt} \int_{\Omega} \phi d\Omega = 0$ is satisfied exactly, but also the conservation of $\frac{d}{dt} \int_{\phi>0} \phi d\Omega$ is at the order of $O(\eta^2)$, better than $O(\eta)$ with

 $W_q(\phi) = 1$. The comparison between the two choices of $W_q(\phi)$ can be found in [7, 35], and the comparison among different conservative Allen-Cahn and Cahn-Hilliard models is available in [38]. It should be noted that the analyses and comparisons in [7, 35, 38] don't include hydrodynamics.

Without the convection term in the left-hand side (LHS) and the last term in the right-hand side (RHS) of Eq.(1), it becomes the original Allen-Cahn equation [3], which is derived from the Ginzburg-Landau free energy,

$$E_F = \int_{\Omega} e_F d\Omega = \int_{\Omega} \lambda \left[\frac{1}{\eta^2} g(\phi) + \frac{1}{2} |\nabla \phi|^2 \right] d\Omega.$$
 (7)

The chemical potential, which is the functional derivative of the free energy, reads

$$\xi = \frac{\delta E_F}{\delta \phi} = \lambda \left[\frac{1}{\eta^2} g'(\phi) - \nabla^2 \phi \right], \tag{8}$$

and the first two terms in the right-hand side (RHS) of Eq.(1) is equivalent to $-M\xi$.

The order-parameter ϕ works as the phase indicator, such that it takes the value 1 in Phase 1 and -1 in Phase 2. Thus, the density and viscosity of the fluid mixture can be computed as

$$\rho = \frac{\rho_1 + \rho_2}{2} + \frac{\rho_1 - \rho_2}{2}\phi,\tag{9}$$

$$\mu = \frac{\mu_1 + \mu_2}{2} + \frac{\mu_1 - \mu_2}{2}\phi,\tag{10}$$

where ρ_1 and μ_1 are the density and viscosity of Phase 1, and ρ_2 and μ_2 are those of Phase 2. Thus, the mass conservation, i.e., $\frac{d}{dt} \int_{\Omega} \rho d\Omega = 0$, is implied by the conservation constraint on the order parameter, i.e., $\frac{d}{dt} \int_{\Omega} \phi d\Omega = 0$.

2.2 The momentum equation and consistency conditions

The motion of different fluid phases is governed by the momentum equation

$$\frac{\partial(\rho \mathbf{u})}{\partial t} + \nabla \cdot (\mathbf{m} \otimes \mathbf{u}) = -\nabla p + \nabla \cdot \left[\mu(\nabla \mathbf{u} + \nabla \mathbf{u}^T) \right] + \rho \mathbf{g} + \mathbf{f}_s + \mathbf{S}_{\mathbf{u}}, \tag{11}$$

where **m** is the mass flux, p is the pressure to enforce the divergence-free condition, i.e., Eq.(2), \mathbf{f}_s is the surface force, which models the effect of surface tension, \mathbf{g} is the gravitational acceleration, and $\mathbf{S}_{\mathbf{u}}$ is the external momentum source.

It should be noted that the single-phase dynamics should be recovered by the momentum equation Eq.(11) away from the interface. For example, in the bulk-phase region of Phase 1, the single-phase incompressible Navier-Stokes equation with density ρ_1 and viscosity μ_1 , i.e.,

$$\frac{\partial(\rho_1\mathbf{u})}{\partial t} + \nabla \cdot (\rho_1\mathbf{u} \otimes \mathbf{u}) = -\nabla p + \mu_1\nabla^2\mathbf{u} + \rho_1\mathbf{g} + \mathbf{S_u},$$

should be reduced from the momentum equation Eq.(11). Specifically in this example, $\mathbf{m} = \rho_1 \mathbf{u}$, $\nabla \cdot (\mu_1(\nabla \mathbf{u})^T) = \mathbf{0}$, and $\mathbf{f}_s = \mathbf{0}$ should be true in the bulk-phase region of Phase 1. This property to recover the single-phase dynamics is called the *consistency of reduction*.

The momentum equation should also be compatible with the mass conservation equation of the model, which is achieved by appropriately choosing the mass flux **m**. Since the density of the fluid mixture is computed from Eq.(9), along with Eq.(1), the mass conservation equation of the model can be written as

$$\frac{\partial \rho}{\partial t} + \nabla \cdot \mathbf{m} = S_m,\tag{12}$$

where S_m is the mass source. Depending on the definition of \mathbf{m} , the corresponding S_m can be determined from Eq.(9) and Eq.(1). An appropriate mass flux should lead to a zero mass source, i.e., $S_m = 0$, see the analyses in [22], and this condition is called the *consistency of mass conservation*. To honor the physical

coupling between the mass and momentum transport, the mass fluxes in the mass conservation equation Eq.(12) and in the momentum equation Eq.(11) should be the same. This condition is called the *consistency* of mass and momentum transport.

To summarize, three consistency conditions are considered, which are

- Consistency of reduction: the two-phase flow model should be able to recover the single-phase dynamics away from the interface, i.e., $\mathbf{m} = \rho \mathbf{u}$, $\nabla \cdot (\mu(\nabla \mathbf{u})^T) = \mathbf{0}$, and $\mathbf{f}_s = \mathbf{0}$, where ρ and μ are either ρ_1 and μ_1 or ρ_2 and μ_2 .
- Consistency of mass conservation: the mass conservation equation should be consistent with one defined from the Phase-Field equation and the density of the fluid mixture. The consistent mass flux \mathbf{m} in the mass conservation equation should lead to a zero mass source, i.e., $S_m \equiv 0$.
- Consistency of mass and momentum transport: the mass flux in the inertial term of the momentum equation should be the consistent mass flux obtained from the mass conservation equation.

These three consistency conditions are proposed in our previous work [22] for two-phase flows using the Cahn-Hilliard model and are extended and applied to N-phase flows in [23]. The analyses and numerical experiments show the significance of satisfying the consistency conditions in both continuous and discrete levels. However, those analyses and schemes work only for the Phase-Field equations that can be written in a conservative form, but the conservative Allen-Cahn equation Eq.(1) is outside the category. If we directly applied the consistency conditions to Eq.(1), we obtain a non-zero mass source, i.e., $S_m = \frac{\rho_1 - \rho_2}{2} \left(-\frac{M\lambda}{\eta^2} g'(\phi) + W_q(\phi) q(t) \right)$, which violates the consistency of mass conservation. As shown in [22], a non-zero mass source interferes with the physical momentum and kinetic energy transport in the continuous level. In the discrete level, it introduces unphysical interface deformation and velocity fluctuations, and, as a result, triggers numerical instability. These effects become more significant as the density difference between the two phases increases. The consistent formulation in the upcoming section is proposed to resolve this issue.

2.3 The consistent formulation

In order to satisfy the consistency conditions when the conservative Allen-Cahn equation Eq.(1) is used to model two-phase flows, the consistent formulation is proposed. We introduce an auxiliary variable Q, which satisfies

$$\nabla \cdot (W_Q(\phi)\nabla Q) = -\frac{M\lambda}{\eta^2}g'(\phi) + W_q(\phi)q(t), \tag{13}$$

where $W_Q(\phi)$ is the weight function for Q. Along with the homogeneous Neumann boundary condition for Q, i.e., $\mathbf{n} \cdot \nabla Q = 0$, Eq.(13) is eligible and solvable by noticing that from the left-hand-side (LHS) of Eq.(13)

$$\int_{\Omega} \nabla \cdot (W_Q \nabla Q) d\Omega = \int_{\partial \Omega} W_Q(\phi) \mathbf{n} \cdot \nabla Q d\Gamma = 0, \tag{14}$$

and from the right-hand-side (RHS) of Eq.(13)

$$-\int_{\Omega} \frac{M\lambda}{\eta^2} g'(\phi) d\Omega + q(t) \int_{\Omega} W_q(\phi) d\Omega = 0, \tag{15}$$

after applying the definition of q(t), i.e., Eq.(5). Although the choice of W_Q can be multiple, we let $W_Q = W_q$ so that q(t) and ∇Q share the same effective region.

Thanks to Eq.(13), the conservative Allen-Cahn equation Eq(1) is reformulated in a conservative form

$$\frac{\partial \phi}{\partial t} + \nabla \cdot \mathbf{m}_{\phi} = 0, \tag{16}$$

where \mathbf{m}_{ϕ} is the Phase-Field flux, defined as

$$\mathbf{m}_{\phi} = \mathbf{u}\phi - M\lambda\nabla\phi - W_{Q}(\phi)\nabla Q. \tag{17}$$

As a result, all the analyses in our previous works [22, 23] are valid for the reformulated equation Eq.(16), and the consistent mass flux can be straightforwardly obtained from the consistency analysis as

$$\mathbf{m} = \frac{\rho_1 + \rho_2}{2} \mathbf{u} + \frac{\rho_1 - \rho_2}{2} \mathbf{m}_{\phi}. \tag{18}$$

We refer interested readers to [22, 23] for detailed analyses and derivations.

The consistent mass flux, defined in Eq.(18), satisfies the consistency of mass conservation. By using Eq.(9), Eq.(2), and Eq.(16), it can be easily shown that

$$\frac{\partial \rho}{\partial t} + \nabla \cdot \mathbf{m} = \frac{\rho_1 - \rho_2}{2} \left(\frac{\partial \phi}{\partial t} + \nabla \cdot \mathbf{m}_{\phi} \right) = 0. \tag{19}$$

In order to satisfy the *consistency of mass and momentum transport*, the consistent mass flux Eq.(18) is applied in the inertial term of the momentum equation. The significance of using the consistent mass flux in the momentum equation has been analyzed and validated in [22], and not repeated here.

The surface force is derived from the energy law. Eq.(1) is multiplied by $\left(\xi - \frac{W_q(\phi)}{M}q(t)\right)$, and then we obtain the equation for the free energy per unite volume e_F ,

$$\frac{\partial e_F}{\partial t} + \mathbf{u} \cdot (\xi \nabla \phi) - \nabla \cdot \left(\lambda \frac{\partial \phi}{\partial t} \nabla \phi + \mathbf{u} \frac{W_q(\phi)}{M} q(t) \right) = -M \left(\xi - \frac{W_q(\phi)}{M} q(t) \right)^2, \tag{20}$$

where $W_q'(\phi) = W_q(\phi)$, and we have used $\frac{\partial W_q(\phi)}{\partial t} = 0$ [32] and the divergence-free condition, i.e., Eq.(2). The equation of the kinetic energy per unite volume, $e_K = \frac{1}{2}\rho \mathbf{u} \cdot \mathbf{u}$, is obtained by the dot product of \mathbf{u} and Eq.(11), i.e.,

$$\frac{\partial e_K}{\partial t} + \nabla \cdot (\mathbf{m} \frac{1}{2} \mathbf{u} \cdot \mathbf{u}) = -\nabla \cdot (\mathbf{u} p) + \nabla \cdot \left[\mu (\nabla \mathbf{u} + \nabla \mathbf{u}^T) \cdot \mathbf{u} \right] - \frac{1}{2} \mu (\nabla \mathbf{u} + \nabla \mathbf{u}^T) : (\nabla \mathbf{u} + \nabla \mathbf{u}^T) + \mathbf{u} \cdot \mathbf{f}_s, \tag{21}$$

and we have used the mass conservation equation, i.e., Eq.(19), and the divergence-free condition, i.e., Eq.(2). The total energy, i.e., $\int_{\Omega} (e_K + e_F) d\Omega$ is governed by the summation of Eq.(20) and Eq.(21). After assuming all the flux terms vanished at the domain boundary, we obtain

$$\frac{\partial}{\partial t} \int_{\Omega} (e_K + e_F) d\Omega = -\frac{1}{2} \int_{\Omega} \mu(\nabla \mathbf{u} + \nabla \mathbf{u}^T) : (\nabla \mathbf{u} + \nabla \mathbf{u}^T) d\Omega - \int_{\Omega} M \left(\xi - \frac{W_q(\phi)}{M} q(t) \right)^2 d\Omega, \tag{22}$$

by requiring the surface force to be

$$\mathbf{f}_s = \xi \nabla \phi. \tag{23}$$

The physical explanation of Eq.(23) is that the work done by the surface force should balance the change of the free energy by convection [26]. The same result can be derived from the least-action principle [57, 73]. Notice that the surface force in Eq.(23) has the same form as the one in the Cahn-Hilliard model [22], and thus, it can be shown that the surface force defined in Eq.(23) is equivalent to a conservative form $\nabla \cdot (-\lambda \nabla \phi \otimes \nabla \phi)$ with the free energy and the chemical potential defined in Eq.(7) and Eq.(8) [28, 26, 57, 23]. As a result, from the momentum equation Eq.(11), the momentum of the two-phase system is conserved. It should be noted that if the consistency conditions are violated, the mass conservation equation, i.e., Eq.(19), does not hold. As a result, an unphysical source term, which is proportional to the density difference of the fluid phases, will appear in Eq.(21) as well as Eq.(22). Consequently, the energy law is violated.

So far, the consistent mass flux Eq.(18) and the surface force Eq.(23) have been derived from the consistency analysis and the energy law, respectively, with the help of the consistent formulation. Therefore the momentum equation Eq.(11) is complete. The last analysis is on the consistency of reduction. Far away from the interface, i.e., $|\nabla \phi| = 0$, ϕ takes the value 1 (or -1). From Eq.(1), we obtain $\frac{\partial \phi}{\partial t} = 0$, since the velocity is divergence-free, g'(1) = 0 (g'(-1) = 0) and $W_q(1) = 0$ ($W_q(-1) = 0$). Thus, ϕ remains to be 1 (or -1) and the Phase-Field flux becomes $\mathbf{m}_{\phi} = \mathbf{u}$ (or $-\mathbf{u}$) from Eq.(17), thanks to $W_Q(1) = 0$ ($W_Q(-1) = 0$). Then, we obtain the mass flux to be $\mathbf{m} = \rho_1 \mathbf{u}$ (or $\rho_2 \mathbf{u}$) from Eq.(18), which is the mass flux of the single-phase flow

where the fluid density is ρ_1 (or ρ_2). Therefore, the consistent mass flux, defined in Eq.(18), satisfies the consistency of reduction. Further, we can immediately obtain $\mathbf{f}_s = \mathbf{0}$ from Eq.(23) due to $|\nabla \phi| = \mathbf{0}$, $\rho = \rho_1$ (or ρ_2) from Eq.(9), and $\mu = \mu_1$ (or μ_2) from Eq.(10). Noticing that $\nabla \cdot (\mu(\nabla \mathbf{u})^T) = \mu \nabla (\nabla \cdot \mathbf{u}) = \mathbf{0}$ from Eq.(2) due to $\mu = \mu_1$ (or μ_2), the momentum equation Eq.(11) becomes

$$\frac{\partial(\rho\mathbf{u})}{\partial t} + \nabla \cdot (\rho\mathbf{u} \otimes \mathbf{u}) = -\nabla p + \mu \nabla^2 \mathbf{u} + \rho \mathbf{g} + \mathbf{S}_{\mathbf{u}}, \tag{24}$$

where ρ and μ take either ρ_1 and μ_1 or ρ_2 and μ_2 . Eq.(24) is exactly the single-phase incompressible Navier-Stokes equation with the corresponding phase density and viscosity. Thus, the single-phase dynamics is recovered away from the interface, and consequently, the *consistency of reduction* is satisfied by the momentum equation Eq.(11). From the above analysis, the *consistency of reduction* casts an additional constraint on $W_q(\phi)$ and $W_Q(\phi)$ that $W_q(\pm 1) = W_Q(\pm 1) = 0$. As a result, using the conservative Allen-Cahn equation with $W_q(\phi) \equiv 1$ violates the *consistency of reduction*.

2.4 Summary of the proposed model for two-phase flows

In summary, the locations of the fluid phases are described by the conservative Allen-Cahn equation Eq.(1). Thanks to the consistent formulation, the conservative Allen-Cahn equation, whose original form is a convection-diffusion-reaction equation, is reformulated into a conservative form by introducing the auxiliary variable Q and Eq.(13). As a result, the consistent mass flux Eq.(18) is derived from the consistency analysis, and the surface force is derived from the energy law of the two-phase system. Finally, the monument equation is coupled with the Phase-Field equation through material properties, i.e., Eq.(9) and Eq.(10), the consistent mass flux Eq.(18), and the surface force Eq.(23). We show that, with our choice of $W_q(\phi)$ and $W_Q(\phi)$, the whole system satisfies the consistency of reduction, the consistency of mass conservation, the consistency of mass and momentum transport, the mass and momentum conservation, and the energy law.

3 Discretization

In this section, we introduce the scheme to solve the governing equations in Section 2. We consider the collocated-grid arrangement, where the order parameter, velocity components and pressure are stored at cell centers (x_i, y_j) and, additionally, the cell-face velocity, which is the velocity component normal to cell faces, is stored at cell faces $(x_{i+1/2}, y_j)$ and $(x_i, y_{j+1/2})$. Details of the spatial discretization and the treatments of different kinds of boundary conditions are available in [22]. In summary, we use the 5th-order WENO scheme [30] for the convective-type operators and the 2nd-order central difference for the diffusive-type and gradient operators.

The major focus will be on the scheme for the conservative Allen-Cahn equation Eq.(1) and on the properties of the scheme. To solve the momentum equation Eq.(11) along with the incompressibility constrain Eq.(2), we use the 2nd-order semi-implicit projection scheme, which has been successfully applied in two-phase flows [22] and in N-phase flows [23].

3.1 Scheme for the conservative Allen-Cahn equation

A three-step scheme is developed to solve the conservative Allen-Cahn equation Eq.(1). Step1: solve the provisional order parameter ϕ^* at all the cell centers (x_i, y_j) from

$$\frac{\gamma_t \phi^* - \hat{\phi}}{\Delta t} + \tilde{\nabla} \cdot (\mathbf{u}^{*,n+1} \tilde{\phi}^{*,n+1}) = M \lambda \tilde{\nabla} \cdot \tilde{\nabla} \phi^* - \frac{M \lambda}{n^2} \tilde{g}'(\phi^*), \tag{25}$$

with the homogeneous Neumann boundary condition, i.e., $\mathbf{n} \cdot \tilde{\nabla} \phi^* = 0$ used, unless otherwise stated. In Eq.(25), γ_t and the linear operator $\widehat{(\cdot)}$ depend on the time discretization scheme, and, unless otherwise specified, we use the 2nd-order backward difference, i.e., $\gamma_t = 1.5$ and $\widehat{(\cdot)} = 2(\cdot)^n - 0.5(\cdot)^{n-1}$, where $(\cdot)^n$ represents the data at time level t^n . $(\cdot)^{*,n+1}$ approximates $(\cdot)^{n+1}$ with the previous time level data, and we use the 2nd-order extrapolation, i.e., $(\cdot)^{*,n+1} = 2(\cdot)^n - (\cdot)^{n-1}$. $\tilde{\nabla} \cdot (\cdot)$ and $\tilde{\nabla} (\cdot)$ are the discrete divergence

and gradient operators, whose definitions are in [22] and not repeated here. $\tilde{(\cdot)}$ represents the result of the WENO scheme. $\tilde{g}'(\phi^*)$ is approximating $g'(\phi^*)$ with Taylor expansion, i.e.,

$$\tilde{g}'(\phi^*) = g'(\phi^n) + g''(\phi^n)(\phi^* - \phi^n). \tag{26}$$

It should be noted that Eq.(25) is solving the original Allen-Cahn equation, which doesn't include the Lagrange multiplier.

Step2: compute the Lagrange multiplier q^* from

$$q^* = \frac{\sum_{i,j} \left[\frac{M\lambda}{\eta^2} \tilde{g}'(\phi^*) \Delta \Omega \right]_{i,j}}{\sum_{i,j} \left[W_q(\phi^n) \Delta \Omega \right]_{i,j}},\tag{27}$$

where $\Delta\Omega$ is the volume of the discrete cells.

Step3: Update the order parameter at n+1 time level at all the cell centers (x_i, y_j) from

$$\frac{\gamma_t \phi^{n+1} - \gamma_t \phi^*}{\Delta t} = W_q(\phi^n) q^*. \tag{28}$$

In Eq.(28), we input ϕ^n , instead of $\phi^{*,n+1}$, to $W_q(\phi)$ because ϕ^n is bounded in [-1,1] with the help of the boundedness mapping algorithm introduced in Section 3.6. $\phi^{*,n+1}$, which is the 2nd-order extrapolation, can be outside [-1,1] and result in a negative weight value, even though both ϕ^n and ϕ^{n-1} are bounded in [-1,1]. So far, we complete the scheme for the conservative Allen-Cahn equation.

Before solving the momentum equation Eq.(11), the consistent mass flux in the discrete level has to be specified first. Thus, the consistent formulation needs to be applied. The auxiliary variable Q is solved at all the cell centers (x_i, y_j) from

$$\tilde{\nabla} \cdot \left(\overline{W_Q(\phi^{n+1})} \tilde{\nabla} Q \right) = -\frac{M\lambda}{\eta^2} \tilde{g}'(\phi^*) + W_q(\phi^n) q^*, \tag{29}$$

where (\cdot) represents the linear interpolation, with the homogeneous boundary condition, i.e., $\mathbf{n} \cdot \nabla Q = 0$, unless otherwise specified. It should be noted that both sides of Eq.(29) are zero away from the interface, which leads to all-zero rows in the coefficient matrix of the discretized linear system of Eq.(29). In practice, to avoid getting all-zero rows, W_Q in Eq.(29) is set to be a small value δ_Q where $|\phi^{n+1}|$ is larger than $(1-\delta_Q)$, due to $W_Q(1-\delta_Q) \sim \delta_Q$. Consequently, Eq.(29) reduces to the Laplace equation, i.e., $\tilde{\nabla} \cdot \tilde{\nabla} Q = 0$, away from the interface, and the gradient of Q becomes zero there. It should be noted that such a modification of W_Q is effective only far away from the interface and it does not change the behavior of Eq.(29) there since $\overline{W_Q}\tilde{\nabla}Q$ is still zero away from the interface. Although Eq.(29) is a variable-coefficient elliptic equation, after the modification of W_Q , most of the rows in the coefficient matrix is representing the discretized Laplace equation, which has constant coefficients and is diagonally dominant, since the domain is majorly occupied by the bulk-phase regions away from the interface. We choose δ_Q to be 10^{-6} since the locations where $|\phi^{n+1}|$ is larger than $(1-10^{-6})$ are about 10η away from the interface. This is adequately far away from the interface, considering that the length scale of the computational domain is about 100η normally. In the present study, all the linear systems are solved to the round-off error by the direct solver in MATLAB, i.e., the "\" operator. It takes about 15% of the time in each time step to solve the conservative Allen-Cahn equation with the scheme in Section 3.1, which includes one matrix inversion, about 20% to solve the consistent formulation, i.e., Eq. (29), which includes again one matrix inversion, and about 65% to solve the momentum equation with the scheme in Section 3.2, which includes three matrix inversions for two-dimensional problems. Therefore, the cost of solving Eq.(29) is similar to solving other linear systems in the scheme.

Finally, at each cell face $(x_{i+1/2}, y_j)$ or $(x_i, y_{j+1/2})$, the discrete Phase-Field flux is

$$\tilde{\mathbf{m}}_{\phi} = \mathbf{u}^{*,n+1} \tilde{\phi}^{*,n+1} - M\lambda \tilde{\nabla} \phi^* - \overline{W_Q(\phi^{n+1})} \tilde{\nabla} Q, \tag{30}$$

which is the discrete counterpart of Eq.(17).

3.2 Scheme for the momentum equation with the incompressibility constrain

We summarize the scheme, proposed in our previous work [22], for the momentum equation with the incompressibility constraint.

Step1: Solve the provisional velocity \mathbf{u}^* at cell centers (x_i, y_j) from

$$\frac{\gamma_t \rho^{n+1} \mathbf{u}^* - \widehat{\rho} \widehat{\mathbf{u}}}{\Delta t} + \widetilde{\nabla} \cdot (\widetilde{\mathbf{m}} \otimes \widetilde{\mathbf{u}}^{*,n+1}) = \rho^{n+1} \overline{\mathbf{G}^n} + \widetilde{\nabla} \cdot \left(\overline{\mu^{n+1}} \widetilde{\nabla} \mathbf{u}^* \right) + \widetilde{\nabla} \cdot \left(\overline{\mu^{n+1}} (\widetilde{\nabla} \widetilde{\mathbf{u}}^{*,n+1})^T \right). \tag{31}$$

Step2: Solve another provisional velocity \mathbf{u}^{**} at cell centers (x_i, y_j) from

$$\frac{\gamma_t \mathbf{u}^{**} - \gamma_t \mathbf{u}^*}{\Delta t} = -\overline{\mathbf{G}^n}.$$
 (32)

Step3: Solve the provisional velocity \mathbf{u}^* at cell faces $(x_{i+1/2}, y_j)$ and $(x_i, y_{j+1/2})$ from

$$\frac{\gamma_t \mathbf{u}^* - \gamma_t \overline{\mathbf{u}^{**}}}{\Delta t} = -\frac{1}{\overline{\rho^{n+1}}} \tilde{\nabla} p^n + \mathbf{G}_s^{n+1}. \tag{33}$$

Step4: Solve the pressure correction p' at cell centers (x_i, y_j) from

$$\frac{\gamma_t}{\Delta t} (\tilde{\nabla} \cdot \mathbf{u}^{n+1} - \tilde{\nabla} \cdot \mathbf{u}^*) = -\tilde{\nabla} \cdot \left(\frac{1}{\overline{\rho^{n+1}}} \tilde{\nabla} p' \right), \tag{34}$$

with the incompressibility constraint in the discrete level, i.e.,

$$\tilde{\nabla} \cdot \mathbf{u}^{n+1} = 0. \tag{35}$$

Step5: Solve p^{n+1} , the pressure at the new time level, at cell centers (x_i, y_i) from

$$p^{n+1} = p^n + p'. (36)$$

Step6: Solve the cell-face velocity at the new time level, i.e., \mathbf{u}^{n+1} at cell faces $(x_{i+1/2}, y_j)$ and $(x_i, y_{j+1/2})$ from

$$\frac{\gamma_t \mathbf{u}^{n+1} - \gamma_t \mathbf{u}^*}{\Delta t} = -\frac{1}{\rho^{n+1}} \tilde{\nabla} p', \tag{37}$$

Step7: Solve the cell-center velocity at the new time level, i.e., \mathbf{u}^{n+1} at cell centers (x_i, y_i) from

$$\frac{\gamma_t \mathbf{u}^{n+1} - \gamma_t \mathbf{u}^{**}}{\Delta t} = \overline{\mathbf{G}^{n+1}}.$$
(38)

In the above steps, ρ^{n+1} and μ^{n+1} are computed from Eq.(9) and Eq.(10), respectively, with ϕ^{n+1} obtained in Section 3.1. The consistent mass flux in the discrete level is

$$\tilde{\mathbf{m}} = \frac{\rho_1 + \rho_2}{2} \mathbf{u}^{*,n+1} + \frac{\rho_1 - \rho_2}{2} \tilde{\mathbf{m}}_{\phi},\tag{39}$$

where the discrete Phase-Field flux $\tilde{\mathbf{m}}_{\phi}$ is available from Eq.(30) after solving the conservative Allen-Cahn equation. Both \mathbf{G} and $\mathbf{G}_{\mathbf{s}}$ are defined at the cell faces $(x_{i+1/2}, y_j)$ and $(x_i, y_{j+1/2})$. $\mathbf{G}_{\mathbf{s}}$ has the form

$$\mathbf{G}_s = \frac{1}{\rho} \mathbf{f}_s + \mathbf{g} + \frac{1}{\rho} \mathbf{S}_{\mathbf{u}},\tag{40}$$

and G is

$$\mathbf{G} = -\frac{1}{\overline{\rho}}\tilde{\nabla}p + \mathbf{G_s}.\tag{41}$$

The surface force can be discretized by either the balanced-force method or the conservative method, which are proposed in [23]. Specifically, in two-phase flows, the balanced-force method reads

$$\mathbf{f}_s = \overline{\xi} \tilde{\nabla} \phi = \lambda \left(\frac{1}{\eta^2} g'(\phi) - \tilde{\nabla} \cdot \tilde{\nabla} \phi \right) \tilde{\nabla} \phi, \tag{42}$$

and the conservative method reads

$$\mathbf{f}_s = \lambda \left(\frac{1}{\eta^2} \tilde{\nabla} g(\phi) - \overline{\tilde{\nabla} \cdot \tilde{\nabla} \phi} \tilde{\nabla} \phi \right). \tag{43}$$

So far, we completed the scheme for solving the momentum equation with the incompressibility constraint. The boundary conditions for the velocity and pressure are problem-dependent and will be specified in individual cases in Section 4.

3.3 Formal order of accuracy

The fully-discretized equations for the conservative Allen-Cahn equation and the momentum equation are

$$\frac{\gamma_t \phi^{n+1} - \hat{\phi}}{\Delta t} + \tilde{\nabla} \cdot (\mathbf{u}^{*,n+1} \tilde{\phi}^{*,n+1}) = M \lambda \tilde{\nabla} \cdot \tilde{\nabla} \phi^* - \frac{M \lambda}{\eta^2} \tilde{g}'(\phi^*) + W_q(\phi^n) q^*, \tag{44}$$

and

$$\frac{\gamma_t \rho^{n+1} \mathbf{u}^{n+1} - \widehat{\rho} \widehat{\mathbf{u}}}{\Delta t} + \tilde{\nabla} \cdot \left(\tilde{\mathbf{m}} \otimes \tilde{\mathbf{u}}^{*,n+1} \right) = \rho^{n+1} \overline{\mathbf{G}^{n+1}} + \tilde{\nabla} \cdot \left(\overline{\mu^{n+1}} \tilde{\nabla} \mathbf{u}^* \right) + \tilde{\nabla} \cdot \left(\overline{\mu^{n+1}} (\tilde{\nabla} \tilde{\mathbf{u}}^{*,n+1})^T \right). \tag{45}$$

The formal order of accuracy of the momentum equation is 2nd-order, which has been analyzed and numerically validated in [22].

Outside the interfacial region, there is no contribution from the Lagrange multiplier, and we have $\phi^{n+1} = \phi^*$. In Eq.(44), $(\phi^{n+1} - \phi^{*,n+1}) \sim O(\Delta t^2)$ and from Eq.(26) $(\tilde{g}'(\phi^*) - g'(\phi^*)) \sim O(\phi^* - \phi^n)^2 \sim O(\Delta t^2)$. In addition, the correction introduced by the Lagrange multiplier is effective only in the interfacial region, which occupies a small portion of the domain, and is expected to be small in one time step. As a result, the scheme for the conservative Allen-Cahn equation is expected to be 2nd-order accurate, which is examined numerically in Section 4.1.1.

3.4 Consistency in the discrete level

In this section, we show that the proposed scheme satisfies the consistency conditions, which are the consistency of reduction, the consistency of mass conservation and the consistency of mass and momentum transport, in the discrete level.

3.4.1 Consistency of reduction

We define the location far away from the interface to be the one where $\phi^n = \phi^{n-1} = 1$ (or -1) is true in its neighborhood. We are going to show that the single-phase dynamics is recovered in this location. We only consider the case of $\phi^n = \phi^{n-1} = 1$ and the case of $\phi^n = \phi^{n-1} = -1$ is the same.

consider the case of $\phi^n = \phi^{n-1} = 1$ and the case of $\phi^n = \phi^{n-1} = -1$ is the same. Based on the given condition, we can immediately obtain $\phi^{*,n+1} = 1$, $\tilde{\phi}^{*,n+1} = 1$ and $\hat{\phi} = \gamma_t$. Since the cell-face velocity is divergence-free at all the time levels, i.e., Eq.(35), we obtain $\tilde{\nabla} \cdot (\mathbf{u}^{*,n+1}\tilde{\phi}^{*,n+1}) = \tilde{\nabla} \cdot \mathbf{u}^{*,n+1} = 2\tilde{\nabla} \cdot \mathbf{u}^n - \tilde{\nabla} \cdot \mathbf{u}^{n-1} = 0$. As a result, from Eq.(25), we have $\phi^* = 1$, by noticing that $g'(\phi^n) = g'(1) = 0$ and $g''(\phi^n) = g''(1) = 2$. Since $W_q(\phi^n) = W_q(1) = 0$, we have $\phi^{n+1} = \phi^* = 1$, from Eq.(28).

Consequently, we can obtain $\rho = \rho_1$ and $\mu = \mu_1$ from Eq.(9) and Eq.(10), respectively, $\tilde{\mathbf{m}}_{\phi} = \mathbf{u}^{*,n+1}$ from Eq.(30) thanks to $W_Q(\phi^{n+1}) = W_Q(1) = 0$, $\tilde{\mathbf{m}} = \rho_1 \mathbf{u}^{*,n+1}$ from Eq.(39), and $\mathbf{f}_s^{n+1} = \mathbf{0}$ due to $\tilde{\nabla}\phi^{n+1}$ and $\tilde{\nabla}g(\phi^{n+1})$ are zero. For the viscous terms, we have $\tilde{\nabla}\cdot\left(\overline{\mu^{n+1}}\tilde{\nabla}\mathbf{u}^*\right) + \tilde{\nabla}\cdot\left(\overline{\mu^{n+1}}(\tilde{\nabla}\tilde{\mathbf{u}}^{*,n+1})^T\right) = \mu_1\tilde{\nabla}\cdot\tilde{\nabla}\mathbf{u}^* + \mu_1\tilde{\nabla}\left(\tilde{\nabla}\cdot\mathbf{u}^{*,n+1}\right) = \mu_1\tilde{\nabla}\cdot\tilde{\nabla}\mathbf{u}^*$. The scheme that grantees $\tilde{\nabla}\cdot(\tilde{\nabla}\tilde{\mathbf{u}}^{*,n+1})^T = \overline{\tilde{\nabla}\left(\tilde{\nabla}\cdot\mathbf{u}^{*,n+1}\right)}$

is designed in our previous work [22]. Combine everything together, and the fully-discretized momentum equation Eq.(45) becomes

$$\frac{\gamma_t \rho_1 \mathbf{u}^{n+1} - \rho_1 \hat{\mathbf{u}}}{\Delta t} + \tilde{\nabla} \cdot (\rho_1 \mathbf{u}^{*,n+1} \otimes \tilde{\mathbf{u}}^{*,n+1}) = \overline{(-\tilde{\nabla} p^{n+1} + \rho_1 \mathbf{g} + \mathbf{S_u}^{n+1})} + \mu_1 \tilde{\nabla} \cdot \tilde{\nabla} \mathbf{u}^*, \tag{46}$$

which is exactly the fully-discretized incompressible Navier-Stokes equation with constant density ρ_1 and viscosity μ_1 . Consequently, away from the interface, the single-phase dynamics is recovered in the discrete level. In other words, the *consistency of reduction* is satisfied in the discrete level.

3.4.2 Consistency of mass conservation

We first consider the identity

$$\frac{\gamma_t \phi^{n+1} - \hat{\phi}}{\Delta t} + \tilde{\nabla} \cdot \tilde{\mathbf{m}}_{\phi} = \frac{\gamma_t \phi^{n+1} - \hat{\phi}}{\Delta t} + \tilde{\nabla} \cdot (\mathbf{u}^{*,n+1} \tilde{\phi}^{*,n+1}) - M\lambda \tilde{\nabla} \cdot \tilde{\nabla} \phi^* - \tilde{\nabla} \cdot (W_Q(\phi^{n+1}) \tilde{\nabla} Q) \qquad (47)$$

$$= \frac{\gamma_t \phi^{n+1} - \hat{\phi}}{\Delta t} + \tilde{\nabla} \cdot (\mathbf{u}^{*,n+1} \tilde{\phi}^{*,n+1}) - M\lambda \tilde{\nabla} \cdot \tilde{\nabla} \phi^* + \frac{M\lambda}{\eta^2} g'(\phi^*) - W_q(\phi^n) q^* = 0,$$

which is the discrete counterpart of Eq.(16), and we have used Eq.(29) and Eq.(44). Then it is straightforward to show that

$$\frac{\gamma_t \rho^{n+1} - \hat{\rho}}{\Delta t} + \tilde{\nabla} \cdot \tilde{\mathbf{m}} = \frac{\rho_1 + \rho_2}{2} \left(\frac{\gamma_t - \hat{1}}{\Delta t} + \tilde{\nabla} \cdot \mathbf{u}^{*,n+1} \right) + \frac{\rho_1 - \rho_2}{2} \left(\frac{\gamma_t \phi^{n+1} - \hat{\phi}}{\Delta t} + \tilde{\nabla} \cdot \tilde{\mathbf{m}}_{\phi} \right) = 0, \quad (48)$$

which is the discrete counterpart of Eq.(19), and we have used $\hat{1} = \gamma_t$, $\tilde{\nabla} \cdot \mathbf{u}^{*,n+1} = 0$, and Eq.(47).

3.4.3 Consistency of mass and momentum transport

The consistent mass flux in the discrete level Eq.(39) has been applied in Eq.(45) and thus the consistency of mass and momentum transport is satisfied in the discrete level. This is important to honor the following physical configuration. We consider the case without viscosity and surface tension, where the initial velocity and pressure are homogeneous, i.e., $\mathbf{u}|_{t=0} = \mathbf{u}_0$ and $p|_{t=0} = p_0$. This initial configuration will persist, i.e., $\mathbf{u} \equiv \mathbf{u}_0$ and $p \equiv p_0$, $\forall t > 0$, since there is no relative motion and the net force acting on the fluid is zero. We can show that, as long as the consistency conditions are satisfied, this physical configuration is maintained in the discrete level, independent of the initial shape of the interface, the density ratio, and the number of phases. We refer interested readers to [23] for the complete proof.

3.5 Conservation in the discrete level

In this section, we consider the mass and momentum conservation of the proposed scheme in the discrete level. Only the periodic domain is considered and, as a result, the summation of the discrete divergence operator over all the cells is zero, i.e., $\sum_{i,j} [\tilde{\nabla} \cdot (\cdot) \Delta \Omega]_{i,j} = 0$, which is shown in [22, 23].

3.5.1 Mass conservation

From Eq.(9), the mass conservation is implied by showing that ϕ is conserved in the discrete level. Given $\sum_{i,j} [\phi^n \Delta \Omega]_{i,j} = \sum_{i,j} [\phi^{n-1} \Delta \Omega]_{i,j} = \dots = \sum_{i,j} [\phi^0 \Delta \Omega]_{i,j}$, we are going to show that $\sum_{i,j} [\phi^{n+1} \Delta \Omega]_{i,j} = \sum_{i,j} [\phi^0 \Delta \Omega]_{i,j}$. From the given condition, we can immediately obtain $\sum_{i,j} \widehat{[\phi \Delta \Omega]_{i,j}} = \gamma_t \sum_{i,j} [\phi^0 \Delta \Omega]_{i,j}$. The summation of the fully-discretized conservative Allen-Cahn equation Eq.(44) over all the cells is

$$\frac{\gamma_t \sum_{i,j} [\phi^{n+1} \Delta \Omega]_{i,j} - \sum_{i,j} \widehat{[\phi \Delta \Omega]_{i,j}}}{\Delta t} = -\sum_{i,j} [\frac{M\lambda}{\eta^2} \widetilde{g}'(\phi^*) \Delta \Omega]_{i,j} + q^* \sum_{i,j} [W_q(\phi^n) \Delta \Omega]_{i,j} = 0, \tag{49}$$

and we have used Eq.(27). As a result, we obtain $\sum_{i,j} [\phi^{n+1} \Delta \Omega]_{i,j} = \sum_{i,j} [\phi^0 \Delta \Omega]_{i,j}$, which implies the mass conservation in the discrete level.

3.5.2 Momentum conservation

The momentum conservation is considered by summing the fully-discretized momentum equation Eq.(45) over all the cells. Noticing that the remaining term $\sum [\rho \overline{\mathbf{G}} \Delta \Omega]$ satisfies $\sum [\rho \overline{\mathbf{G}} \Delta \Omega] = \sum [\overline{\rho} \mathbf{G} \Delta \Omega] = \sum [(-\tilde{\nabla} p + \mathbf{f}_s)\Delta \Omega] = \sum [\mathbf{f}_s \Delta \Omega]$, the momentum is conserved in the discrete level, i.e., $\sum_{i,j} [\rho^{n+1} \mathbf{u}^{n+1} \Delta \Omega]_{i,j} = \sum_{i,j} [\rho^0 \mathbf{u}^0 \Delta \Omega]_{i,j}$, without surface tension, i.e., $\mathbf{f}_s \equiv \mathbf{0}$.

It has been shown in [23] that $\sum[\mathbf{f}_s] = \mathbf{0}$ when using the conservative method, while the balanced-force method performs better on the numerical force balance. In addition, we expect that the non-conservative error introduced by the balanced-force method to be small. First, the surface force is a local force, i.e., it is only non-zero in the interfacial region. Second, the difference between the two methods is from $g'(\phi)\tilde{\nabla}\phi - \tilde{\nabla}g(\phi)$, which has a zero leading order since both $g'(\phi)\tilde{\nabla}\phi$ and $\tilde{\nabla}g(\phi)$ are approximating $\nabla g(\phi)$. Consequently, when using the conservative method, the momentum is conserved in the discrete level even when there is a surface tension, while it is essentially conserved in the discrete level when using the balanced-force method.

The more detailed proof of the momentum conservation of the present scheme for the momentum equation is available in [23] and the proof is generalized for N-phase flows. We refer interested readers to that paper [23].

3.6 A consistent and conservative boundedness mapping algorithm

The conservative Allen-Cahn equation, Eq.(1), honors the maximum principle [2]. Specifically in our case, given $\phi \in [-1,1]$ at t=0, $\phi \in [-1,1]$ at t>0, where ϕ is the solution of Eq.(1). In the discrete level, the maximum principle should be held at every cell and at all the time levels. However, due to a numerical error, the maximum principle may not hold. In numerical practice, we observe that the numerical solution may slightly go beyond the interval [-1,1]. Simply clipping the solution breaks down the consistency and conservation of the scheme. To resolve the issue of violating the maximum principle while maintaining the consistency and conservation of the scheme, we propose a consistent and conservative boundedness mapping algorithm.

Given ϕ^{n+1} , which is the solution of Eq.(44) and satisfies the conservation constraint, i.e., $\sum_{i,j} [\phi^{n+1}\Delta\Omega]_{i,j} = \sum_{i,j} [\phi^0\Delta\Omega]_{i,j}$, we specify a mapping from ϕ^{n+1} to ϕ^b , such that ϕ^b satisfies the maximum principle, i.e., $|\phi^b| \leq 1$ at every cell, the conservation constraint, i.e., $\sum_{i,j} [\phi^b\Delta\Omega]_{i,j} = \sum_{i,j} [\phi^{n+1}\Delta\Omega]_{i,j}$, and the consistency constraint, i.e., $\phi^b = 1$ (or -1) at the locations where $\phi^{n+1} \geq 1$ (or ≤ -1). Since we have shown in Section 3.4.1 that $\phi^{n+1} = 1$ (or -1) inside the bulk-phase region, the out-of-bound solution can first appear only in the interfacial region. The consistency constraint restricts the mapping to be only effective in the interfacial region, and that the mapping doesn't modify the solution in the existing bulk-phase region. This constraint avoids generating fictitious interfaces inside the existing bulk-phase region after the mapping.

Such a mapping from ϕ^{n+1} to ϕ^b can be defined as

$$\phi^{b} = \phi^{b*} + \frac{W_{b}(\phi^{b*})}{\sum_{i,j} [W_{b}(\phi^{b*})\Delta\Omega]_{i,j}} \sum_{i,j} [(\phi^{n+1} - \phi^{b*})\Delta\Omega]_{i,j},$$
(50)

where ϕ^{b*} is the clipped Phase-Field function, i.e.,

$$\phi^{b*} = \begin{cases} 1, \phi^{n+1} \geqslant 1 \\ -1, \phi^{n+1} \leqslant -1 \\ \phi^{n+1}, \text{else} \end{cases} , \tag{51}$$

and $W_b(\phi)$ is a weight function which is non-zero only in the interfacial region. We let $W_b(\phi) = W_q(\phi)$. It is straightforward to show from Eq.(50) that ϕ^b satisfies the conservation constraint, i.e.,

$$\sum_{i,j} [\phi^b \Delta \Omega]_{i,j} = \sum_{i,j} [\phi^{b*} \Delta \Omega]_{i,j} + \frac{\sum_{i,j} [W_b(\phi^{b*}) \Delta \Omega]_{i,j}}{\sum_{i,j} [W_b(\phi^{b*}) \Delta \Omega]_{i,j}} \sum_{i,j} [(\phi^{n+1} - \phi^{b*}) \Delta \Omega]_{i,j} = \sum_{i,j} [\phi^{n+1} \Delta \Omega]_{i,j} = \sum_{i,j} [\phi^0 \Delta \Omega]_{i,j}.$$
(52)

The consistency constraint is also satisfied by ϕ^b . At the locations where $\phi^{n+1} \ge 1$ (or ≤ -1), $\phi^{b*} = 1$ (or -1), from Eq.(51). Since $W_b(\pm 1)$ is zero, $\phi^b = 1$ (or -1) wherever $\phi^{n+1} \ge 1$ (or ≤ -1). Although Eq.(50)

doesn't guarantee the maximum principle, i.e., $\phi_b \in [-1, 1]$, we can iteratively apply Eq.(51) and Eq.(50) sequentially until $|\phi^b| \leq 1$. During the iteration, it should be noted that ϕ^{n+1} in Eq.(51) is replaced by the newly obtained ϕ^b . Notice that the risky locations of $|\phi^b| > 1$ are where $|\phi^{b*}|$ is less but close to 1. However, at those locations, $W_b(\phi^{b*})$ is close to zero. In addition, the difference between ϕ^{b*} and ϕ^{n+1} is small, on the order of truncation error, since the out-of-bound error is introduced by discretization. As a result, the chance of ϕ^b being outside the range [-1,1] is small. We did not observe any need to iterate Eq.(51) and Eq.(50) in numerical practice.

After obtaining ϕ^b from Eq.(50), the consistent formulation is performed once more to enforce the consistency conditions. The following Poisson equation,

$$\tilde{\nabla} \cdot \left(\overline{W_Q(\phi^b)} \tilde{\nabla} \mathcal{Q} \right) = \frac{\gamma_t \phi^b - \gamma_t \phi^{n+1}}{\Delta t},\tag{53}$$

is supplemented. After summing both sides of Eq.(53) over all the cells, the left-hand side (LHS) is zero since both ϕ^b and ϕ^{n+1} satisfy the conservation constraint, and the right-hand side (RHS) is also zero due to the homogeneous Neumann boundary condition. As a result, Eq.(53) is solvable. After replacing ϕ^{n+1} by ϕ^b and $\tilde{\mathbf{m}}_{\phi}$ by $\tilde{\mathbf{m}}_{\phi} - \overline{W}_Q(\phi^b)\tilde{\nabla}Q$, Eq.(47) holds, and, thus, the consistency of mass conservation and the consistency of mass and momentum transport are maintained in the discrete level. Notice that $W_Q(\phi^b) = 0$ inside the bulk-phase region, where $\phi^b = 1$ (or -1), the consistency of reduction is again preserved. The analysis of momentum conservation is not influenced by the boundedness mapping algorithm.

Consequently, the boundedness mapping algorithm is consistent and conservative. It can be directly applied to other high-order schemes for the conservative Allen-Cahn model [39], to other Phase-Field models, e.g., the Cahn-Hilliard model[22] and the conservative Phase-Field model [12], and to the Volume-of-Fluid (VOF) method, whenever the numerical solution needs to be mapped into a physical interval. In the conservative Allen-Cahn model, we can avoid solving the additional Poisson equation Eq.(53) for \mathcal{Q} by combining \mathcal{Q} in Eq.(29) and \mathcal{Q} in Eq.(53) together, i.e.,

$$\tilde{\nabla} \cdot \left(\overline{W_Q(\phi^b)} \tilde{\nabla} Q \right) = -\frac{M\lambda}{n^2} \tilde{g}'(\phi^*) + W_q(\phi^n) q^* + \frac{\gamma_t \phi^b - \gamma_t \phi^{n+1}}{\Delta t}. \tag{54}$$

The methods to sovle Eq.(53) and Eq.(54) are the same as that for Eq.(29).

In summary, the boundedness mapping algorithm is performed after ϕ^{n+1} is solved, and then we obtain ϕ^b . After solving Eq.(54), ϕ^{n+1} is replaced by ϕ^b , and then everything else in Sections 3.1 and 3.2 remains the same.

3.7 Summary of the proposed scheme for two-phase flows

Here, we summarize the consistent, conservative, and bounded scheme for two-phase flows using the conservative Allen-Cahn equation. Given the data at previous time levels, ϕ^{n+1} , \mathbf{u}^{n+1} , and p^{n+1} are obtained from the following steps.

- 1. Solve the conservative Allen-Cahn equation with the scheme, i.e., Eq.(25), Eq.(27), and Eq.(28), in Section 3.1 to obtain ϕ^{n+1} .
- 2. if $\max |\phi^{n+1}| \leq 1$, solve Q from Eq.(29),
 - if $\max |\phi^{n+1}| > 1$, perform the boundedness mapping, i.e., Eq.(51) and Eq.(50), in Section 3.6 to obtain ϕ^b . Iteration might be needed so that $\max |\phi^b| \leq 1$. After that, compute Q from Eq.(54) and then $\phi^{n+1} = \phi^b$.
- 3. Compute ρ^{n+1} from Eq.(9), μ^{n+1} from Eq.(10), $\tilde{\mathbf{m}}$ from Eq.(39), and \mathbf{f}_s^{n+1} from either Eq.(42) or Eq.(43).
- 4. Solve the momentum equation from Eq.(31) to Eq.(38) in Section 3.2 to obtain \mathbf{u}^{n+1} and p^{n+1} .

Then, we can proceed to the next time level.

4 Validations and applications

In this section, we first validate the proposed scheme in Section 4.1, and then we show its capability to model two-phase dynamics in Section 4.2.

4.1 Validations

The formal order of accuracy of the proposed scheme is validated by the manufactured solution problem in Section 4.1.1. The steady drop problem, in Section 4.1.2, is performed to quantify the numerical force balance between the pressure gradient and the surface force which is discretized by either the balanced-force method or the conservative method. The convergence behavior of the numerical Phase-Field solution to the sharp interface solution is studied in Section 4.1.3. The significance of satisfying the consistency conditions is illustrated through the large-density-ratio advection problem in Section 4.1.4. Finally, the mass and momentum conservation and the energy law of the scheme are validated, and the effectiveness of the boundedness mapping algorithm is illustrated by the horizontal shear layer problem in Section 4.1.5. Two more cases, which are the reversed single vortex problem [54] and the Zalesak's disk problem [77], are supplemented in Appendix to validate the conservative Allen-Cahn model as an interface capturing method. Since these two cases are not coupled with the momentum equation, there is no issue related to the consistency conditions. We use h to denote the grid/cell size. The L_2 error is defined as the root mean square of $(f - f_E)$ and the L_{∞} error is the maximum of $|f - f_E|$, where f is the variable of interest and f_E is the corresponding reference value.

4.1.1 Manufactured solution

The manufactured solution problem is performed to validate the formal order of accuracy of the proposed scheme. Specifically, we assume that the exact solutions of the dependent variables are

$$\phi_E = \cos(x)\cos(y)\sin(t),$$

$$Q_E = \cos(x)\cos(y)\sin(t),$$

$$u_E = \sin(x)\cos(y)\cos(t),$$

$$v_E = -\cos(x)\sin(y)\cos(t),$$

$$p_E = \cos(x)\cos(y)\sin(t).$$
(55)

As a result, the following source terms

$$S_{\phi} = \frac{\partial \phi_{E}}{\partial t} + \nabla \cdot (\mathbf{u}_{E}\phi_{E}) - M\lambda \nabla^{2}\phi_{E} + \frac{M\lambda}{\eta^{2}}g'(\phi_{E}) - W_{q}(\phi_{E})q_{E}$$

$$S_{Q} = \nabla \cdot (W_{Q}(\phi_{E})\nabla Q_{E}) + \frac{M\lambda}{\eta^{2}}g'(\phi_{E}) - W_{q}(\phi_{E})q_{E}$$

$$\mathbf{S}_{\mathbf{u}} = \frac{\partial(\rho_{E}\mathbf{u}_{E})}{\partial t} + \nabla \cdot (\mathbf{m}_{E}\otimes\mathbf{u}_{E}) + \nabla p_{E} - \nabla \cdot \left[\mu_{E}(\nabla\mathbf{u}_{E} + \nabla\mathbf{u}_{E}^{T})\right] - \rho_{E}\mathbf{g} - \mathbf{f}_{s}^{E},$$

$$(56)$$

where q_E , ρ_E , μ_E , \mathbf{m}_E and \mathbf{f}_s^E are computed from Eq.(5), Eq.(9), Eq.(10), Eq.(18) and Eq.(23), respectively, are added to the right-hand side (RHS) of Eq.(25), Eq.(29), and Eq.(31), respectively.

The domain considered is $[-\pi,\pi] \times [-\pi,\pi]$ with the free-slip boundary. It should be noted that the exact velocity is divergence-free, i.e., $\nabla \cdot \mathbf{u}_E = 0$, the free-slip boundary condition is consistent with the exact solution, and $\int_{\Omega} \phi_E d\Omega$ is independent of time. The cell size is ranging from $\frac{2\pi}{8}$ to $\frac{2\pi}{128}$. The material properties and parameters are $\rho_1 = 3$, $\rho_2 = 1$, $\mu_1 = 0.02$, $\mu_2 = 0.01$, $\mathbf{g} = \{1, -2\}$, $\eta = 0.1$, $\lambda = 0.001$ and M = 0.001. The initial condition is from the exact solutions Eq.(55) by setting t = 0. All the computations are stopped at t = 1.

In the first case, the time step Δt is fixed to be 0.001 and the spatial convergence is considered. The results of using the balanced-force method are in Table 1 and those using the conservative method are in Table 2. The 2nd-order convergence is clearly observed. We conclude that the proposed scheme is formally 2nd-order accurate in space. In the second case, the time step is proportional to the cell size, i.e., $\Delta t = \frac{h}{2\pi}$. The results of the balanced-force and the conservative methods are listed in Tables 3 and 4, respectively. We

Table 1: Results of the manufactured solution problem using the balanced-force method and $\Delta t = 0.001$

C-: 1		φ				и				1	υ			р			
Grid	L_2	order	L_{∞}	order													
8	2.60e-2	2.15	4.29e-2	1.75	4.09e-2	1.93	8.78e-2	1.32	4.15e-2	1.84	8.06e-2	1.09	1.01e-1	1.40	2.56e-1	1.44	
16	5.85e-3	2.00	1.28e-2	1.86	1.07e-2	1.97	3.53e-2	1.87	1.16e-2	1.97	3.77e-2	1.79	3.82e-2	1.98	9.42e-2	2.00	
32	1.46e-3	2.00	3.51e-3	1.97	2.74e-3	1.99	9.64e-3	1.98	2.95e-3	1.99	1.09e-2	1.95	9.72e-3	2.05	2.36e-2	2.02	
64	3.67e-4	1.99	8.97e-4	1.99	6.86e-4	2.00	2.44e-3	1.99	7.41e-4	2.00	2.82e-3	1.99	2.34e-3	2.04	5.79e-3	2.02	
128	9.21e-5		2.26e-4		1.72e-4		6.12e-4		1.85e-4		7.12e-4		5.70e-4		1.43e-3		

Table 2: Results of the manufactured solution problem using the conservative method and $\Delta t = 0.001$

Grid			φ			и				1	υ			Į.)	
Gild	L_2	order	L_{∞}	order												
8	2.60e-2	2.15	4.29e-2	1.75	4.09e-2	1.93	8.78e-2	1.32	4.15e-2	1.84	8.06e-2	1.09	1.01e-1	1.41	2.56e-1	1.45
16	5.85e-3	2.00	1.28e-2	1.86	1.07e-2	1.97	3.53e-2	1.87	1.16e-2	1.97	3.77e-2	1.79	3.80e-2	1.98	9.37e-2	2.00
32	1.46e-3	2.00	3.51e-3	1.97	2.74e-3	1.99	9.63e-3	1.98	2.95e-3	1.99	1.09e-2	1.95	9.62e-3	2.06	2.34e-2	2.02
64	3.67e-4	1.99	8.97e-4	1.99	6.86e-4	2.00	2.44e-3	1.99	7.41e-4	2.00	2.82e-3	1.99	2.32e-3	2.04	5.75e-3	2.02
128	9.21e-5		2.25e-4		1.72e-4		6.11e-4		1.85e-4		7.13e-4		5.64e-4		1.42e-3	

Table 3: Results of the manufactured solution problem using the balanced-force method and $\Delta t = \frac{h}{2\pi}$

Grid			φ			и				1	υ			Į)	
Grid	L_2	order	L_{∞}	order												
8	3.76e-2	2.21	6.07e-2	1.81	5.11e-2	2.35	1.46e-1	1.99	4.06e-2	1.84	8.32e-2	1.04	1.38e-1	1.76	2.75e-1	1.65
16	8.15e-3	2.06	1.74e-2	1.97	1.00e-2	1.99	3.67e-2	1.94	1.13e-2	2.00	4.04e-2	1.83	4.07e-2	1.88	8.79e-2	1.88
32	1.96e-3	2.03	4.42e-3	1.99	2.52e-3	1.99	9.56e-3	1.99	2.84e-3	2.00	1.13e-2	1.96	1.10e-2	2.06	2.38e-2	2.04
64	4.80e-4	2.01	1.12e-3	2.00	6.36e-4	1.99	2.40e-3	2.00	7.10e-4	2.00	2.91e-3	1.99	2.64e-3	2.06	5.79e-3	2.04
128	1.19e-4		2.79e-4		1.60e-4		5.98e-4		1.78e-4		7.31e-4		6.36e-4		1.40e-3	

Table 4: Results of the manufactured solution problem using the conservative method and $\Delta t = \frac{h}{2\pi}$

Grid		φ			u			v				р				
Gna	L_2	order	L_{∞}	order												
8	3.76e-2	2.21	6.07e-2	1.81	5.11e-2	2.35	1.46e-1	1.99	4.06e-2	1.84	8.32e-2	1.04	1.37e-1	1.77	2.73e-1	1.64
16	8.15e-3	2.06	1.74e-2	1.97	1.00e-2	1.99	3.67e-2	1.94	1.13e-2	2.00	4.04e-2	1.83	4.04e-2	1.89	8.74e-2	1.88
32	1.96e-3	2.03	4.42e-3	1.99	2.52e-3	1.99	9.55e-3	1.99	2.84e-3	2.00	1.13e-2	1.96	1.09e-2	2.06	2.37e-2	2.04
64	4.80e-4	2.01	1.12e-3	2.00	6.36e-4	1.99	2.40e-3	2.00	7.10e-4	2.00	2.92e-3	1.99	2.62e-3	2.06	5.75e-3	2.04
128	1.19e-4		2.79e-4		1.60e-4		5.98e-4		1.78e-4		7.32e-4		6.29e-4		1.39e-3	

again observe 2nd-order convergence, which implies that the proposed scheme is formally 2nd-order accurate in time.

4.1.2 Steady drop

The steady drop problem is performed to quantify the numerical force balance between the pressure gradient and the surface force which is discretized by either the balanced-force method or the conservative method. With a circular interface surrounded by quiescent fluids, in the continuous level, the surface tension is exactly balanced by the pressure jump, and thus the fluid remains stationary. However, such an exact force balance is seldom achievable in the discrete level, and the force imbalance introduced by the discretization drives the fluid to move, generating the so-called spurious current.

We consider the domain of $[1 \times 1]$ with free-slip boundary. A circular drop with a radius 0.2 is placed at the center of the domain and the velocity is initially zero. The cell size is ranging from $\frac{1}{16}$ to $\frac{1}{128}$ and the time step is $\Delta t = 10^{-3}$. The material properties are $\rho_1 = \rho_2 = 1000$, $\mu_1 = \mu_2 = 0.1$, and $\sigma = 1$. The Phase-Field parameters are set up as those in [44, 22], i.e., $\eta = \eta_0 (h/h_0)^{2/3}$ and $M = M_0 (\eta/\eta_0)^{3/2}$, where $\eta_0 = h_0 = 1/32$ and $M_0 = 10^{-7}$. The strength of the spurious current is evaluated at t = 10, by measuring the L_2 and L_∞ norms of the total velocity, i.e., $V = \sqrt{u^2 + v^2}$.

Fig.1 shows the convergence behavior of the total velocity in L_2 and L_{∞} norms. We can observe that the spurious current is small and converges to zero as the cell is refined, no matter which method is used. The balanced-force method has a better performance in achieving the numerical force balance. The spurious

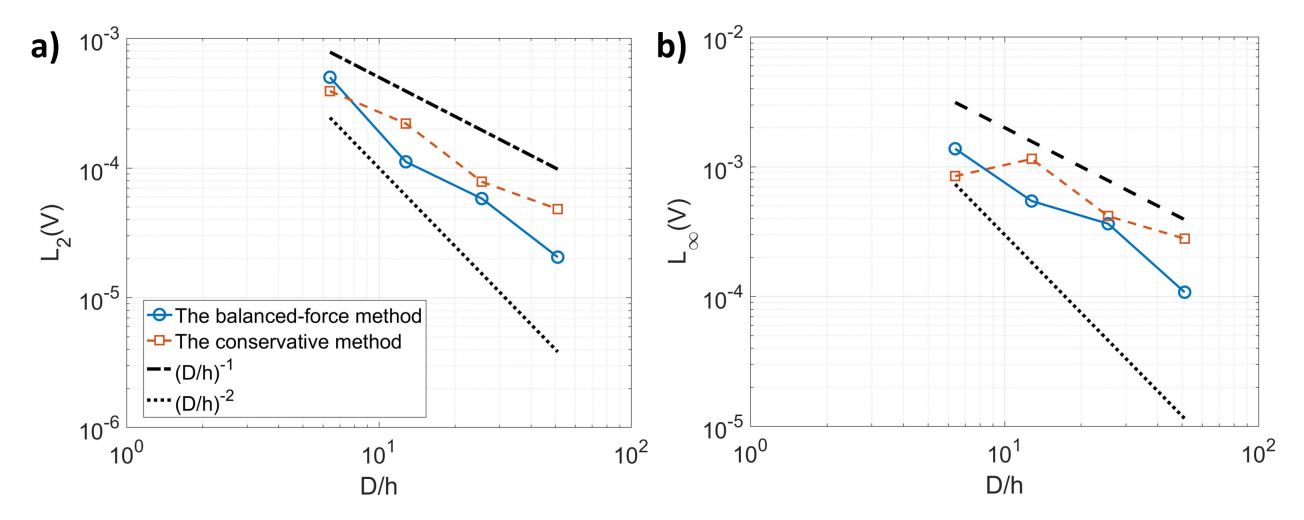


Figure 1: Results of the steady drop problem. a) L_2 norm of V, b) L_{∞} norm of V.

current is smaller than the one from the conservative method. In addition, the spurious current converges to zero with a rate that is close to 2nd-order when using the balanced-force method, while it is more close to 1st-order when the conservative method is applied. The behavior of the two methods observed in the present work is consistent with the results in [23].

4.1.3 Rising bubble: a convergence test

The convergence behavior of the numerical solution of the Phase-Field model to the sharp-interface solution is studied in a problem including large density ratio, large viscosity ratio, surface tension, and gravity. There are two convergence criteria when numerically applying a Phase-Field model to two-phase problems. The first one is the convergence of the numerical solution to the exact solution of the Phase-Field model with fixed interface thickness η by reducing the cell size, which has been studied in Section 4.1.1. The second one is the convergence of the Phase-Field model to the sharp-interface model by reducing the interface thickness η , which, for the conservative Allen-Cahn model, has been studied, e.g., in [7, 10] without hydrodynamics. In this section, we focus on the overall behavior where the interface thickness is reduced as the cell size is reduced.

The domain considered is $[1 \times 2]$, whose left and right boundaries are free-slip and the top and bottom ones are no-slip. The cell size h is ranging from $\frac{1}{16}$ to $\frac{1}{256}$, and the time step is $\Delta t = 0.128h$. A circular bubble (Phase 1) with a radius 0.25 is initially released at (0.5, 0.5) inside a quiescent fluid (Phase 2). The material properties are $\rho_1 = 1$, $\rho_2 = 1000$, $\mu_1 = 0.1$, $\mu_2 = 10$, $\sigma = 1.96$ and $\mathbf{g} = \{0, -0.98\}$. The interface thickness reduces as fast as the cell size, i.e., $\eta = \eta_0(h/h_0)$, where $\eta_0 = h_0 = 1/32$, and the mobility is $M = M_0(\eta/\eta_0)$ with $M_0 = 10^{-7}$. Three benchmark quantities, which are the circularity ψ_c , the center of mass y_c and the rising velocity v_c , are defined as

$$\psi_c = \frac{P_a}{P_b} = \frac{2\sqrt{\int_{\phi>0} \pi d\Omega}}{P_b},\tag{57}$$

$$y_c = \frac{\int_{\Omega} y \frac{1+\phi}{2}}{\int_{\Omega} \frac{1+\phi}{2}},\tag{58}$$

$$v_c = \frac{\int_{\Omega} v \frac{1+\phi}{2}}{\int_{\Omega} \frac{1+\phi}{2}},\tag{59}$$

where P_a is the perimeter of the circle whose area is identical to the bubble, and P_b is the perimeter of the bubble. The sharp-interface solutions using either the Level-Set method or the Arbitrary Lagrangian-Eulerian (ALE) method are available in [24], which are considered as the reference solution.

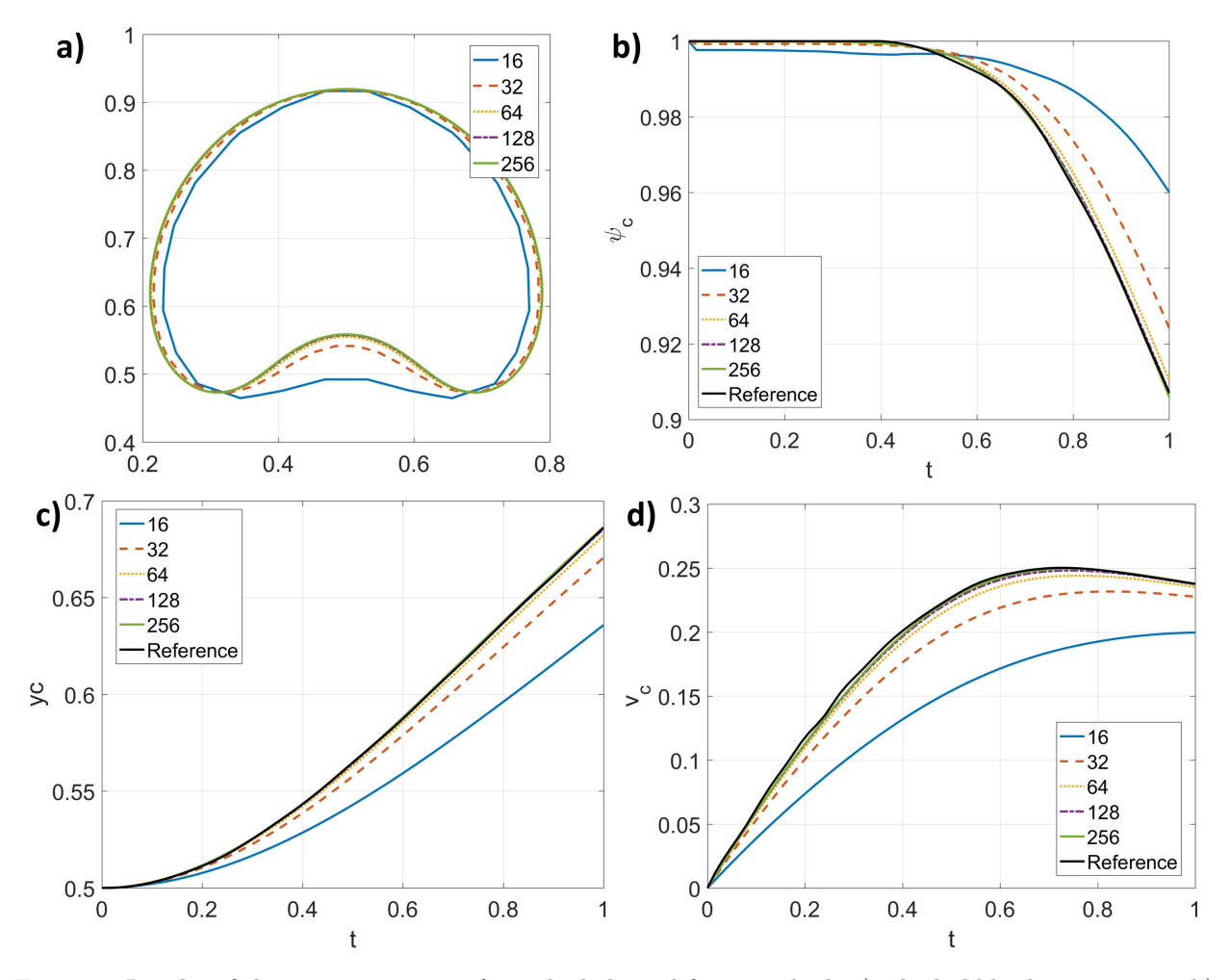


Figure 2: Results of the convergence test from the balanced-force method. a) The bubble shape at t=1, b) ψ_c versus t, c) y_c versus t, and d) v_c versus t. Blue solid line: $h=\frac{1}{16}$, red dashed line: $h=\frac{1}{32}$, yellow dotted line: $h=\frac{1}{32}$, purple dash-dotted line: $h=\frac{1}{128}$, green solid line: $h=\frac{1}{256}$, and black solid line: Reference solution from [24].

Figs.2 and 3 show the results from the balanced-force method and the conservative method, respectively. No matter which method is used, the convergence of the numerical Phase-Field solution to the sharp-interface solution (the Reference) can be clearly observed during successive cell refinement. To quantify the convergence behavior, the L_2 errors of the circularity ψ_c , the center of mass y_c , and the rising velocity y_c are computed, considering the sharp-interface solutions as the reference values, and they are listed in Table 5. The difference between the two methods is tiny although the conservative method slightly outperforms the balanced-force method. The circularity, which quantifies the shape of the bubble, has a convergence rate close to 2nd-order, while it is around 1.6th-order for the center of mass and the rising velocity. In summary, the numerical Phase-Field solution converges to the sharp-interface solution with a rate between 1.5th- and 2nd-order.

In Section 4.1.1, we demonstrate that the scheme is formally 2nd-order accurate although $W(\phi^n)$ is used in Eq.(28). To further investigate its effect on the accuracy of the scheme in a realistic two-phase flow problem, we repeat the convergence test but fix both η and M, i.e., $\eta = \eta_0$ and $M = M_0$, as the grid is refined. As a result, the numerical solution converges to the exact solution of the Phase-Field model. L_2 errors of the benchmark quantities are computed using the finest-grid solution as the reference and are listed in Table 6. We again observe 2nd-order convergence. Therefore, using $W(\phi^n)$ in Eq.(28) has little effect on the accuracy of the scheme. The slowing down of the convergence rate in Table 5 is attributed to

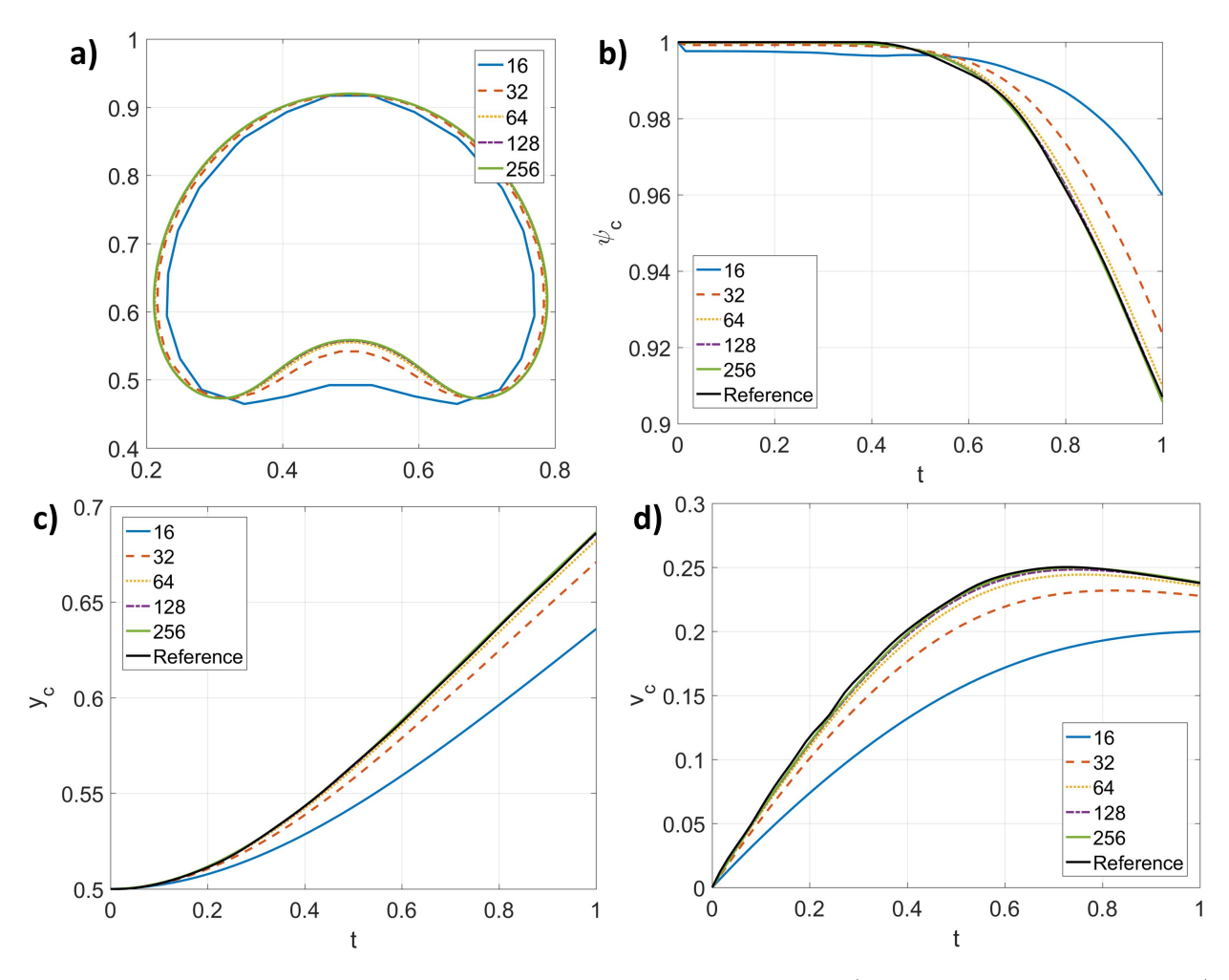


Figure 3: Results of the convergence test from the conservative method. a) The bubble shape at t=1, b) ψ_c versus t, c) y_c versus t, and d) v_c versus t. Blue solid line: $h=\frac{1}{16}$, red dashed line: $h=\frac{1}{32}$, yellow dotted line: $h=\frac{1}{32}$, purple dash-dotted line: $h=\frac{1}{128}$, green solid line: $h=\frac{1}{256}$, and black solid line: Reference solution from [24].

Table 5: L_2 error of the convergence test

		The balanced-force method					The conservative method							
Grid	ψ_c		y_c		v_c		ψ_c		y_c		v_c			
	L_2	order	L_2	order	L_2	order	L_2	order	L_2	order	L_2	order		
16	1.93e-2	1.33	2.84e-2	1.64	5.62e-2	1.55	1.92e-2	1.36	2.83e-2	1.65	5.60e-2	1.56		
32	7.65e-3	1.97	9.09e-3	1.82	1.91e-2	1.52	7.50e-3	2.08	9.02e-3	1.85	1.90e-2	1.55		
64	1.95e-3	1.78	2.58e-3	1.62	6.66e-3	1.12	1.77e-3	1.91	2.50e-3	1.69	6.48e-3	1.17		
128	5.68e-4		8.38e-4		3.06e-3		4.71e-4		7.72e-4		2.89e-3			

approximating a sharp-interface problem with a Phase-Field model.

We then consider the effect of the mobility. We first fix the grid size to be $h = \frac{1}{128}$ but change M_0 from 10^{-3} to 10^{-9} . The results are shown in Fig.4. Although the mobility changes in a wide range, the difference among the solutions is negligible. Therefore, the two-phase flow model shows good tolerance to the value of the mobility. Since the asymptotic analysis of the present two-phase flow model is not available, we have borrowed the analysis to the model using the Cahn-Hilliard equation [26, 27] and related the mobility to the interface thickness as $M = M_0(\eta/\eta_0)$, whose results are shown in Fig.2, Fig.3, and Table 5. The convergence of the numerical solution to the sharp-interface solution has been observed and quantified. Another suggestion

Table 6: L_2 error of the convergence test with fixed η and M

Grie	7	ψ_c		y_c		v_c	
Grie	u	L_2	order	L_2	order	L_2	order
16		3.09e-3	2.35	3.17e-3	3.30	6.69e-3	3.07
				3.23e-4			
64		1.52e-4	2.58	5.91e-5	2.31	3.05e-4	2.18
128	3	2.54e-5		1.19e-5		6.74e-5	

Table 7: L_2 error of the convergence test with $M = M_0(\eta/\eta_0)^2$

Grid	ψ_c		y_c		v_c	
Grid	L_2	order	L_2	order	L_2	order
					5.64e-2	
32	7.67e-3	1.98	8.98e-3	1.81	1.91e-2	1.52
64	1.95e-3	1.78	2.56e-3	1.62	6.66e-3	1.12
128	5.68e-4		8.36e-4		3.06e-3	

is to relate M to η as $M = M_0(\eta/\eta_0)^2$ [42, 71]. Since the model is not sensitive to the mobility, we can infer that changing the correlation of the mobility will not make a big difference in the convergence behavior to the sharp-interface solution, and the results, obtained from $M = M_0(\eta/\eta_0)^2$ with $M_0 = 10^{-3}$, in Table 7, confirm the statement. It should be noted that these observations are based on a practical and numerically affordable set-up and the interface thickness considered is probably not small enough to reach the asymptotic regime. Therefore, they are useful for numerical implementation but not necessarily representing the behavior of the model in the asymptotic regime. Numerically reaching the asymptotic regime is challenging since it normally requires a tremendous number of grid points to resolve the interface thickness which can be a million times smaller than the length scale of the problem [76]. Therefore, the asymptotic analysis is a more appropriate tool to study the behavior of the model inside the asymptotic regime, but it is outside the scope of the present study. Fortunately, we demonstrate that satisfactory results can be obtained even outside the asymptotic regime, which makes the proposed model practical and computationally affordable to study two-phase flows numerically.

4.1.4 Large-density-ratio advection

The large-density-ratio advection problem is performed to validate the analysis in Section 3.4.3, and to illustrate the significance of satisfying the consistency conditions. The domain considered is $[1 \times 1]$ with a periodic boundary condition. A circular drop with a radius 0.1 is initially located at the center of the domain and both the x- and y-components of the velocity are unity. The cell size h is $\frac{1}{128}$ and the time step is $\Delta t = 0.1h$. The fluids are inviscid and there is no surface tension between them. We set $\eta = 3h$ and $M = 10^{-7}$. Based on the analysis of Section 3.4.3, the drop should return to its original location without any deformation, and the velocity should not be changed.

Fig.5 a) shows the result of the density ratio 10^9 from the proposed consistent scheme at t=1. The physical solution is well reproduced. The interface at t=1 is on top of the one at t=0, and the velocity vectors are all pointing towards 45^0 from the x axis. For comparison, the result of the density ratio 10^3 from the inconsistent scheme, i.e., $\tilde{\mathbf{m}} = \overline{\rho} \mathbf{u}$ is depicted in Fig.5 b). One can observe strong compression of the interface along the flow direction and the streamlines are distorted.

4.1.5 Horizontal shear layer

The horizontal shear layer is performed to validate the mass and momentum conservation of the scheme, after which the energy law and the effectiveness of the boundedness mapping algorithm are discussed. The domain considered is $[1 \times 1]$ with a periodic boundary condition. The cell size h is $\frac{1}{128}$ in default and the time step is $\Delta t = \text{CFL}h$, with CFL = 0.1. The material properties are $\rho_1 = 10$, $\rho_2 = 1$, $\mu_1 = 0.01$, $\mu_2 = 0.001$,

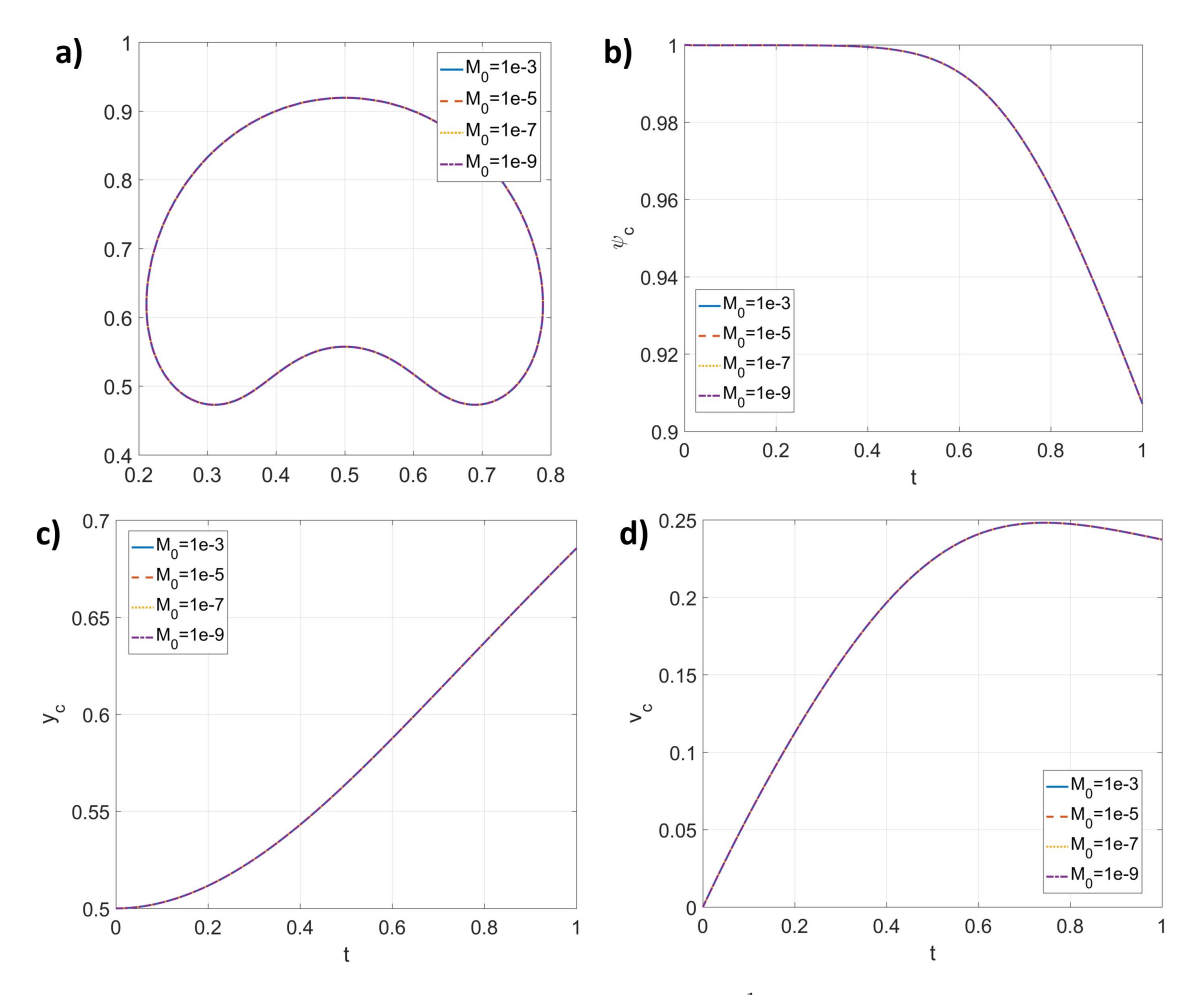


Figure 4: Results of the convergence test with fixed grid size $h = \frac{1}{128}$ but different M_0 . a) The bubble shape at t = 1, b) ψ_c versus t, c) y_c versus t, and d) v_c versus t.

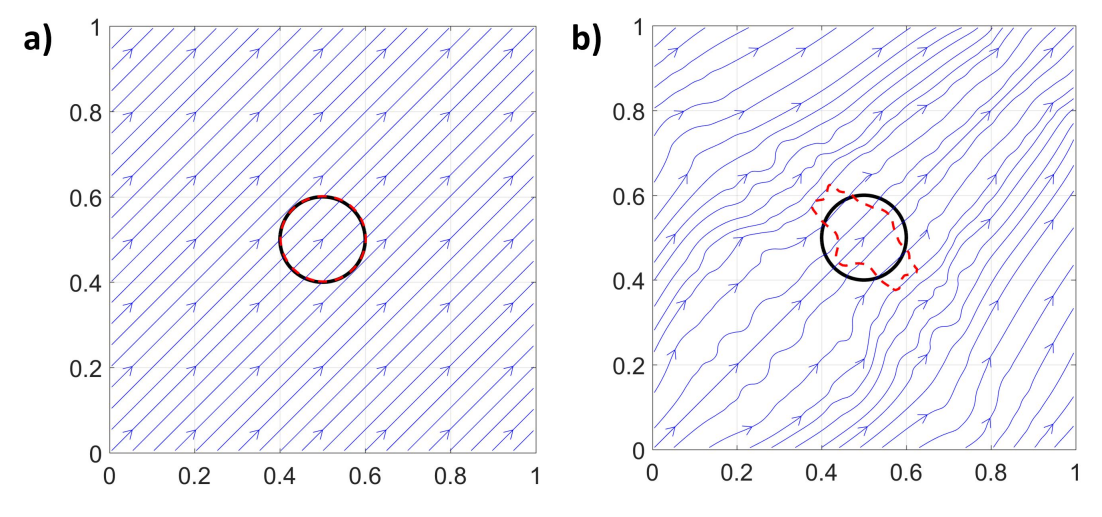


Figure 5: Results of the large-density-ratio advection problem. a) Result from the consistent mass flux with a density ratio 10^9 , b) result from the inconsistent mass flux with a density ratio 10^3 . Black solid line: interface at t = 0, blue arrow lines: streamlines at t = 1, red dashed line: interface at t = 1.

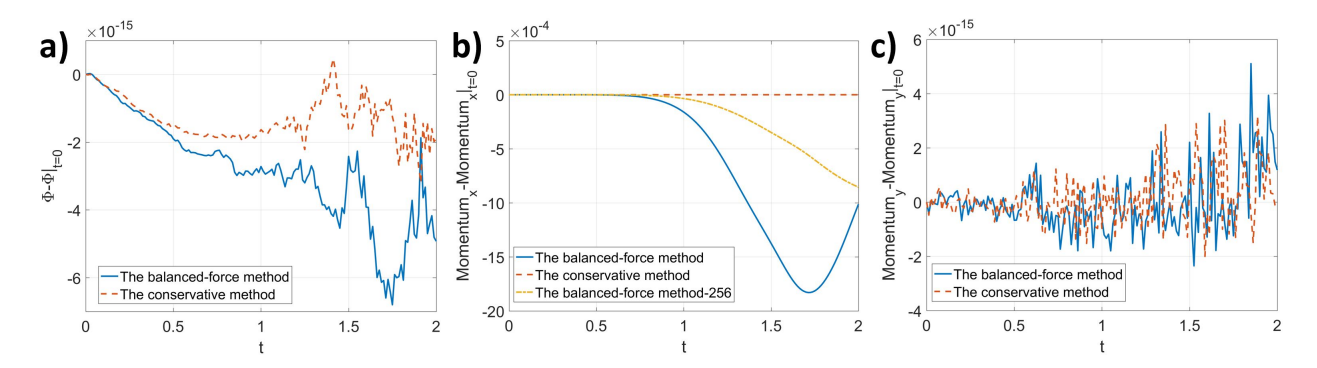


Figure 6: Time histories of the changes of the mass and momentum in the horizontal shear layer problem. a) Change of Φ versus t, b) change of Momentum_x versus t, c) change of Momentum_y versus t. 256: results from a finer grid size $h = \frac{1}{256}$.

 $\sigma = 0.1$. Initially, a horizontal shear layer is

$$u|_{t=0} = \begin{cases} \tanh(\frac{y-y_1}{\delta_1}), y \le y_0 \\ \tanh(\frac{y_2-y}{\delta_1}), y > y_0 \end{cases}$$
 (60)

along with a vertical perturbation

$$v|_{t=0} = \delta_2 \sin(kx),\tag{61}$$

and we set $\phi|_{t=0} = u|_{t=0}$. The parameters are $y_0 = 0.5$, $y_1 = 0.25$, $y_2 = 0.75$, $\delta_1 = 1/30$, $\delta_2 = 0.05$, and as a result, $\eta = \delta_1/\sqrt{2}$.

We first consider the case without performing the boundedness mapping algorithm. The time histories of $\Phi = \sum_{i,j} [\phi \Delta \Omega]_{i,j}$, Momentum_x = $\sum_{i,j} [\rho u \Delta \Omega]_{i,j}$ and Momentum_y = $\sum_{i,j} [\rho v \Delta \Omega]_{i,j}$ minus their initial values are shown in Fig.6. It is clear that the mass is conserved in the discrete level due to Φ is conserved. Since the set up of the problem is symmetric with respect to the y axis, the Momentum_y is also conserved no matter whether the balanced-force method or the conservative method is used. However, Momentum_x is conserved only when the conservative method is used, as expected. A finer grid resolution of the balanced-force method is performed, and the momentum non-conservative error is greatly reduced. Considering the initial value of Momentum_x is 3.9, the maximum change of Momentum_x is less than 0.05% from the default-grid solution. As a result, the scheme using the balanced-force method leads to the essential conservation of momentum. The results in Fig.6 are consistent with our analyses in Sections 3.5.1 and 3.5.2.

The time histories of the kinetic energy, computed by $E_K = \sum_{i,j} [\frac{1}{2}\rho(u^2+v^2)\Delta\Omega]_{i,j}$, the free energy, computed by $E_F = \sum_{i,j} \left[\lambda \left(\frac{1}{\eta^2} g(\phi) + \frac{1}{2} \overline{\tilde{\nabla} \phi \cdot \tilde{\nabla} \phi} \right) \Delta \Omega \right]_{i,j}$, and the total energy, $E_T = E_K + E_F$, are shown in Fig.7. In Fig.7 a), we consider the case without viscosity and surface tension. As a result, the free energy is zero, and the right-hand side (RHS) of the energy law, i.e., Eq.(22), is zero. In other words, the total energy, which is the same as the kinetic energy in this case, should not change with time. The decay of the total energy, as well as the kinetic energy, in Fig. 7 a) is attributed to the numerical dissipation introduced by the backward difference for time discretization, the WENO scheme for the convection terms, and the linear interpolation of the pressure gradient in the momentum equation. The numerical dissipation should be reduced after the grid size is refined, and we can observe that the decay of the energy happens latter and its amount is smaller in a fine-grid solution. The second case is inviscid but it includes the surface tension and the results are shown in Fig. 7 b). From Eq. (22), the total energy decays only due to the second term on the right-hand side (RHS), introduced by the conservative Allen-Cahn model. It can be observed that the decrease of the kinetic energy corresponds to the increase of the free energy. However, the decrease of the kinetic energy is always larger than the increase of the free energy, leading to the decay of the total energy. Fig. 7 c) shows the results of the case including both the viscosity and surface tension. From Eq. (22), the total energy decays due to both the viscosity of the fluids and the conservative Allen-Cahn model. We again observe the energy transfer from the kinetic energy to the free energy and the decay of the total energy.

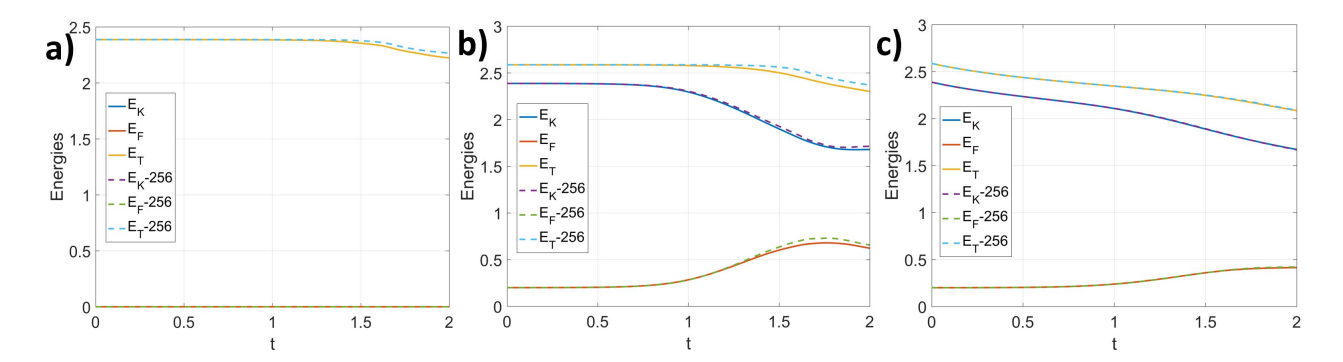


Figure 7: Time histories of the kinetic energy, free energy and total energy in the horizontal shear layer problem using the conservative method. a) without viscosity and surface tension, b) without viscosity but surface tension, c) with viscosity and surface tension. 256: results from a finer grid size $h = \frac{1}{256}$.

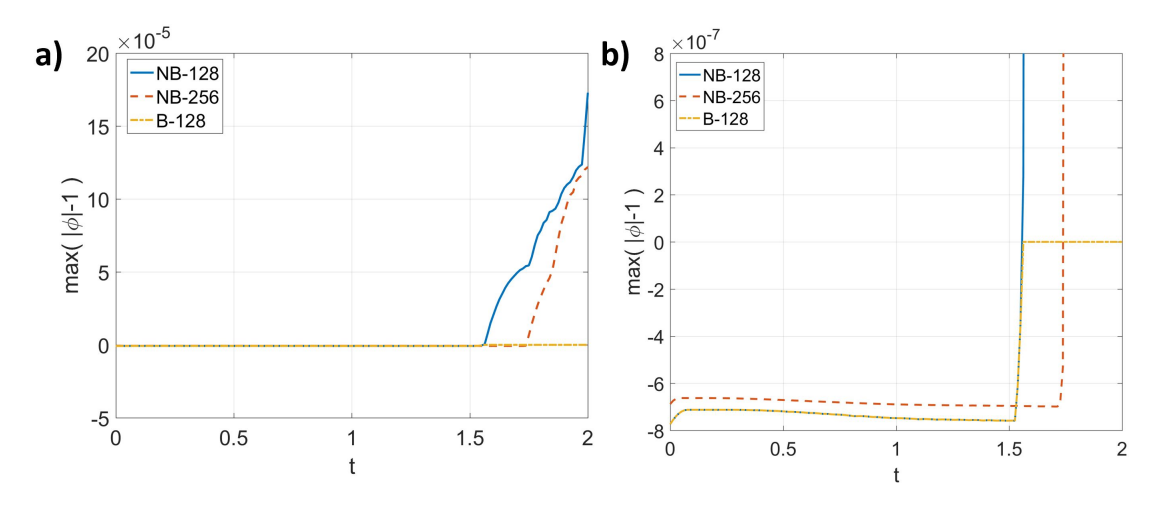


Figure 8: Effectiveness of the boundedness mapping algorithm. a) Time histories of $\max(|\phi|-1)$ using the conservative method, b) zoom of a). NB: the boundedness mapping algorithm is not activated, B: the boundedness mapping algorithm is activated. 128: grid size $h = \frac{1}{128}$, 256: grid size $h = \frac{1}{256}$.

The results from a finer grid are also included in Fig.7 b) and c), and the difference between the fine-grid solution and the default-grid solution is small. Thus, the contribution of the numerical dissipation to the energy decay is negligible. The balanced-force method gives almost identical results so we only present the results from the conservative method. In summary, the energy law, i.e., Eq.(22), is reproduced by the scheme in the discrete level.

The effectiveness of the boundedness mapping algorithm is illustrated in Fig.8, where the time history of $\max(|\phi|-1)$ is shown. From the maximum principle, ϕ should be in the range of [-1,1]. Thus, $\max(|\phi|-1)$ should always be negative. We observe that before t=1.5, ϕ satisfies the maximum principle, and the boundedness mapping algorithm is not activated. After t=1.5, ϕ slightly goes beyond the interval [-1,1] without the boundedness mapping algorithm. When we refine the grid, ϕ stays in [-1,1] longer and the outof-bound error becomes smaller. In Fig.8 b), which is the zoom of Fig.8 a), we observe that before t=1.5, there is no difference between the solutions with and without the boundedness mapping algorithm since the algorithm is not activated. After t=1.5, ϕ remains to be in [-1,1] with the help of the boundedness mapping algorithm while it is outside [-1,1] without the boundedness mapping algorithm. The balanced-force method gives almost identical results so we only present the results from the conservative method. The changes of Φ and momentum versus time are shown in Fig.9 and the boundedness mapping algorithm is included. The boundedness mapping algorithm doesn't change the properties of the mass and momentum conservation of the scheme, which is consistent with our analysis in Section 3.6. The time histories of the kinetic energy,

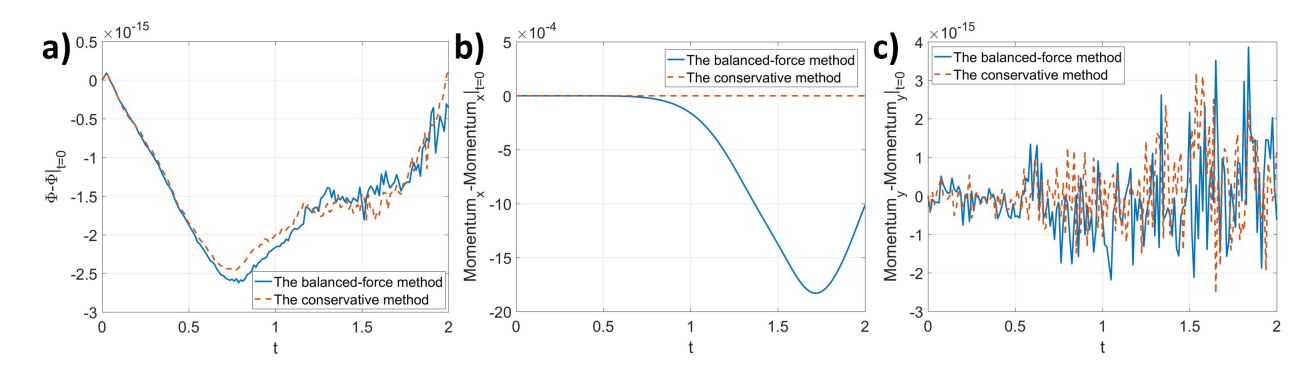


Figure 9: Time histories of the changes of the mass and momentum in the horizontal shear layer problem including the boundedness mapping algorithm. a) Change of Φ versus t, b) change of Momentum_u versus t, c) change of Momentum_u versus t.

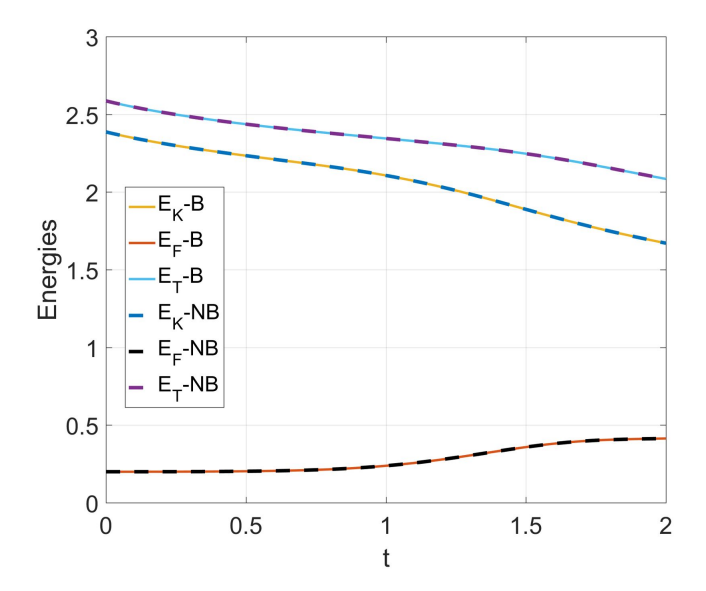


Figure 10: Time histories of the kinetic energy, free energy, and total energy in the horizontal shear layer problem using the conservative method with or without the boundedness mapping algorithm. B: the boundedness mapping algorithm is activated, NB: the boundedness mapping algorithm is not activated.

free energy, and total energy are shown in Fig.10, along with the results without the boundedness mapping algorithm. The energy law is preserved when the boundedness mapping algorithm is included, and there is no observable difference between the results with and without the boundedness mapping algorithm. The balanced-force method gives almost identical results so we only present the results from the conservative method.

4.2 Applications

We apply the proposed scheme to three realistic two-phase flow problems, which are the Rayleigh-Taylor instability, the dam break, and the axisymmetric rising bubble. These problems include different challenging aspects of two-phase flow simulations, e.g., large density and viscosity ratios, surface tension, topological change, and complicated interfacial evolution. Our results show that the proposed scheme is accurate and effective for two-phase flow simulations. Unless otherwise specified, we set $\eta=0.01$ and $M\lambda=10^{-7}$ in this section.

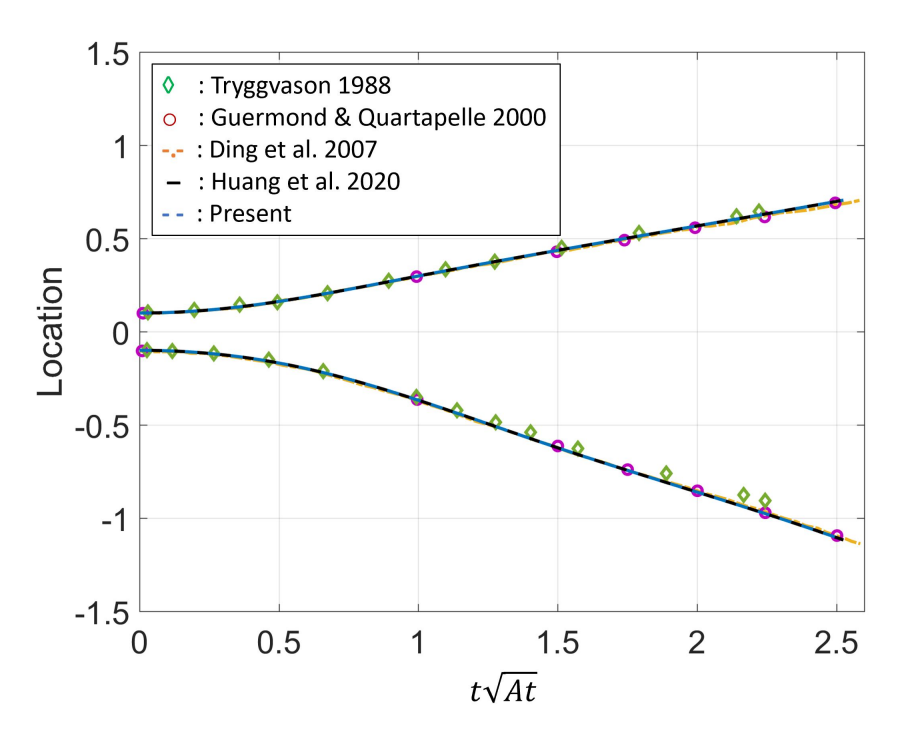


Figure 11: The locations of the interface at the center and the lateral edge of the domain for the Rayleigh-Taylor instability problem.

4.2.1 Rayleigh-Taylor instability

The Rayleigh-Taylor instability problem is presented, where the surface tension is ignored. When a heavier fluid (Phase 1) stays above a lighter one, any small perturbation on the interface will trigger the instability where the heavier fluid moves downward, taking the place of the lighter one. The domain considered is $[1 \times 4]$, whose left and right boundaries are periodic and the top and bottom ones are free-slip. The heavier fluid stays on the upper half of the domain and the interface is initially perturbed by a sinusoidal wave whose amplitude and wavenumber are 0.1 and 2π , respectively. The material properties $\rho_1 = 3$, $\rho_2 = 1$, $\mu_1 = \mu_2 = 10^{-3}$, and $\mathbf{g} = \{0, -1\}$, which leads to an Atwood number $At = \frac{\rho_1 - \rho_2}{\rho_1 + \rho_2} = 0.5$. The domain is discretized by $[128 \times 512]$ cells and the time step is $\Delta t = 5 \times 10^{-4} / \sqrt{At}$.

The early dynamics of the problem is quantified by measuring the locations of the interface at the center and at the lateral edge of the domain versus time, which is presented in Fig.11, along with the results from [65, 19, 13, 22]. The present results agree very well with the previous studies. The evolution of the interface is shown in Fig.12 up to $t\sqrt{At} = 10$. The amplitude of the initial perturbation keeps growing, and a secondary instability is triggered at the two sides of the front of the heavier fluid after $t\sqrt{At} = 1.25$. As a result, the interface has a mushroom-like shape. As the heavier fluid moves downward, some small structures are generated by the instability. Further, there are new instabilities appearing on the small structures, resulting in topological changes. Consequently, we can observe a complicated interface configuration in the long-time dynamics of the problem.

4.2.2 Dam break

The dam break problem is presented, where a square water column collapses due to gravity. The domain considered is $[4a \times 2a]$, where a is the initial height of the water column (Phase 1), and all the boundaries are no-slip. Initially, a square water column stays at the left of the domain, having a height and a width a = 5.715 cm (2.25in). The density and viscosity of the water are 998.207kg/m^3 and $1.002 \times 10^{-3} \text{Pa} \cdot \text{s}$, and they are 1.204kg/m^3 and $1.78 \times 10^{-5} \text{Pa} \cdot \text{s}$ for the air. The surface tension between them is $\sigma = 7.28 \times 10^{-2} \text{N/m}$ and the gravity is 9.8m/s^2 , pointing downward. The equations are non-dimensionalized by a density scale 1.204kg/m^3 , a length scale 5.715 cm, and a acceleration scale 9.8m/s^2 . The domain is discretized by $[256 \times 128]$

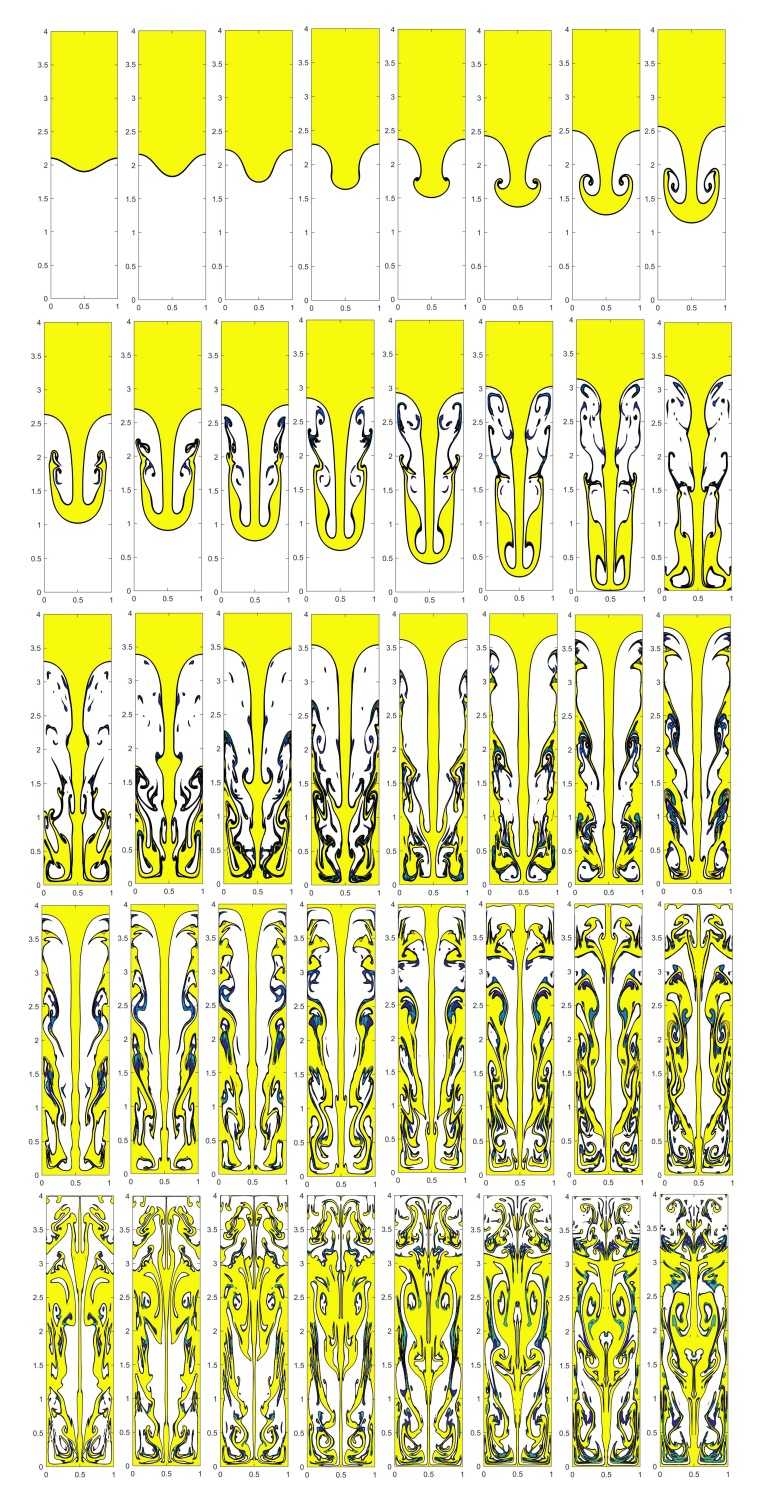


Figure 12: The evolution of the interface of the Rayleigh-Taylor instability problem at $t\sqrt{At}=0, t\sqrt{At}=0.5, t\sqrt{At}=0.75, t\sqrt{At}=1,..., t\sqrt{At}=10$ from left to right and from top to bottom.

cells and the time step is $\Delta t = 10^{-4}$. Both the balanced-force method and the conservative method are applied to this problem.

The early dynamics of the problem is quantified by measuring the front and the height of the water column versus time, which is presented in Fig.13, along with the experimental data from [43]. The results

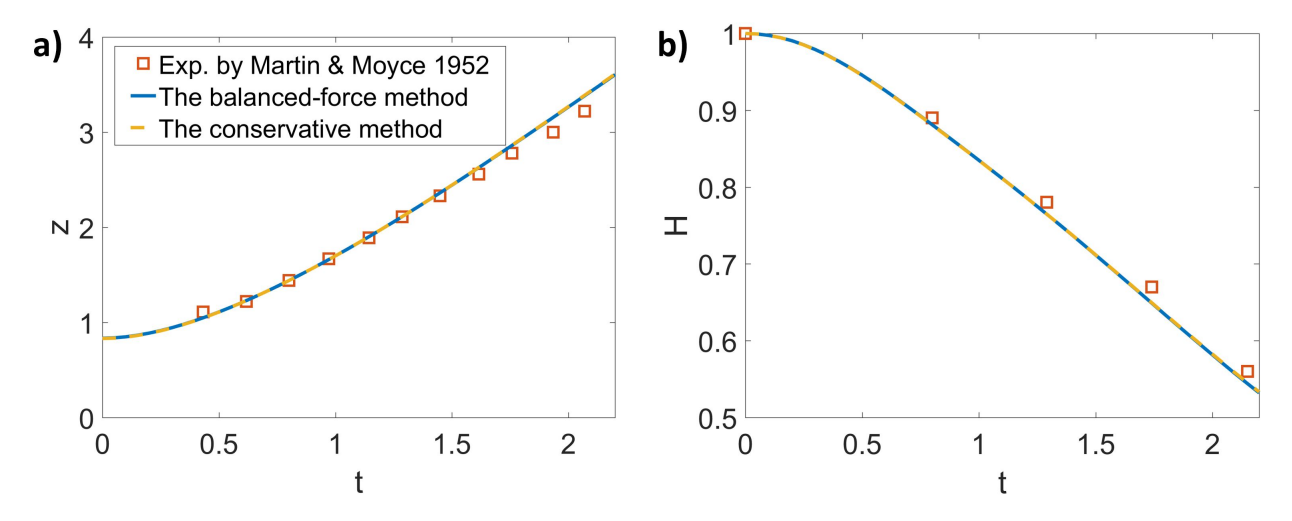


Figure 13: The front and the height of the water column versus time. a) The front of the water column versus time, b) the height of the water column versus time

from the balanced-force method and from the conservative method overlap with each other, and both of them agree well with the experimental measurements. The evolution of the interface is shown in Fig.14 up to t=10, where both of the results from the two methods are presented. The water column collapses towards the right of the domain and climbs up the right wall. The rising motion is slowed down by gravity, while the water at the bottom is still pushed upward. As a result, there is a bump in the middle of the climbing water. This bump collapses onto the bottom water and pushes it moving backward. Consequentially, a water jump is developed and moves toward the left, along with complicated interface configurations. At the end of the simulation, the water jump reaches the left wall and the bottom water is pushed to move to the right again. Although both the balanced-force method and the conservative method give a similar physical picture of the problem, it can be observed that the balanced-force method tends to break the interface when the length scale of the interfacial structure is close to the cell size. As a result, more topological changes are observed in the results using the balanced-force method. Our results also show that the conservative method is more stable than the balanced-force method. We use a time step that is 5 times larger, and the conservative method is stable for the whole simulation, while the balanced-force method is only stable before the water touches the top wall.

4.2.3 Axisymmetric rising bubble

The axisymmetric rising bubble is presented to show the applicability of our consistent scheme to other coordinate systems. A spherical bubble with a radius R is released at z=2R in an axisymmetric domain $[4R\times 8R]$ with a free-slip boundary condition at z=0, z=8R, and r=4R. We consider R=0.01m, the density of the liquid is $\rho_L=1000 {\rm kg/m^3}$, and the gravity along the negative z axis is $g_z=10 {\rm m/s^2}$. Other parameters are specified as the density ratio 1000, the viscosity ratio 100, the Bond number $Bo=\frac{\rho_L g_z R^2}{\sigma}=200$, and the Reynolds number $Re=\frac{\rho_L R \sqrt{g_z R}}{\mu_L}=100$. The equations are non-dimensionalized by using R, ρ_L and g_z as the length, density and acceleration scales. The domain is discretized by $[200\times 400]$ cells, and the time step is $\Delta t=10^{-3}$.

Figs.15 and 16 show the results from the balanced-force method and the conservative method, respectively. In this case, both of the methods give the same evolution of the bubble. The buoyancy effect drives the bubble upward. The bottom part of the bubble moves faster, and at the end catches up with its top. As a result, the topological change happens, and the bubble becomes a band ring. The present results are comparable to those in [62], where the same case is considered using the Level-Set method.

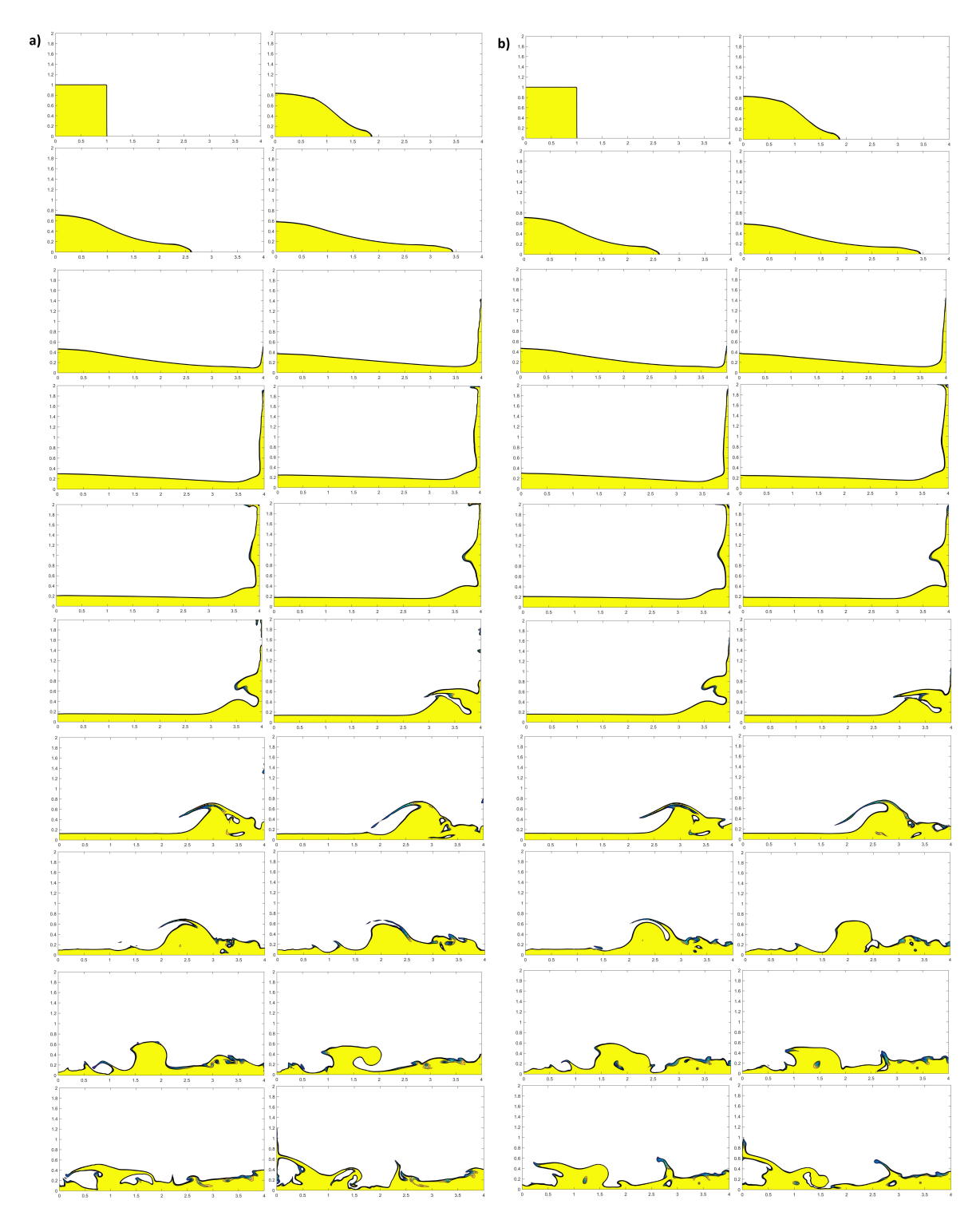


Figure 14: The evolution of the interface of the dam break problem at t = 0, t = 1, t = 1.5, t = 2, t = 2.5,..., t = 10 from left to right and from top to bottom. a) The balanced-force method, b) the conservative method.

5 Discussions

5.1 Extension to multiphase flows

Recently, Kim and Lee have extended the conservative Allen-Cahn equation Eq.(1) to the conservative vector-valued Allen-Cahn equation [34] which is used to model multiphase flows. In this section, we are

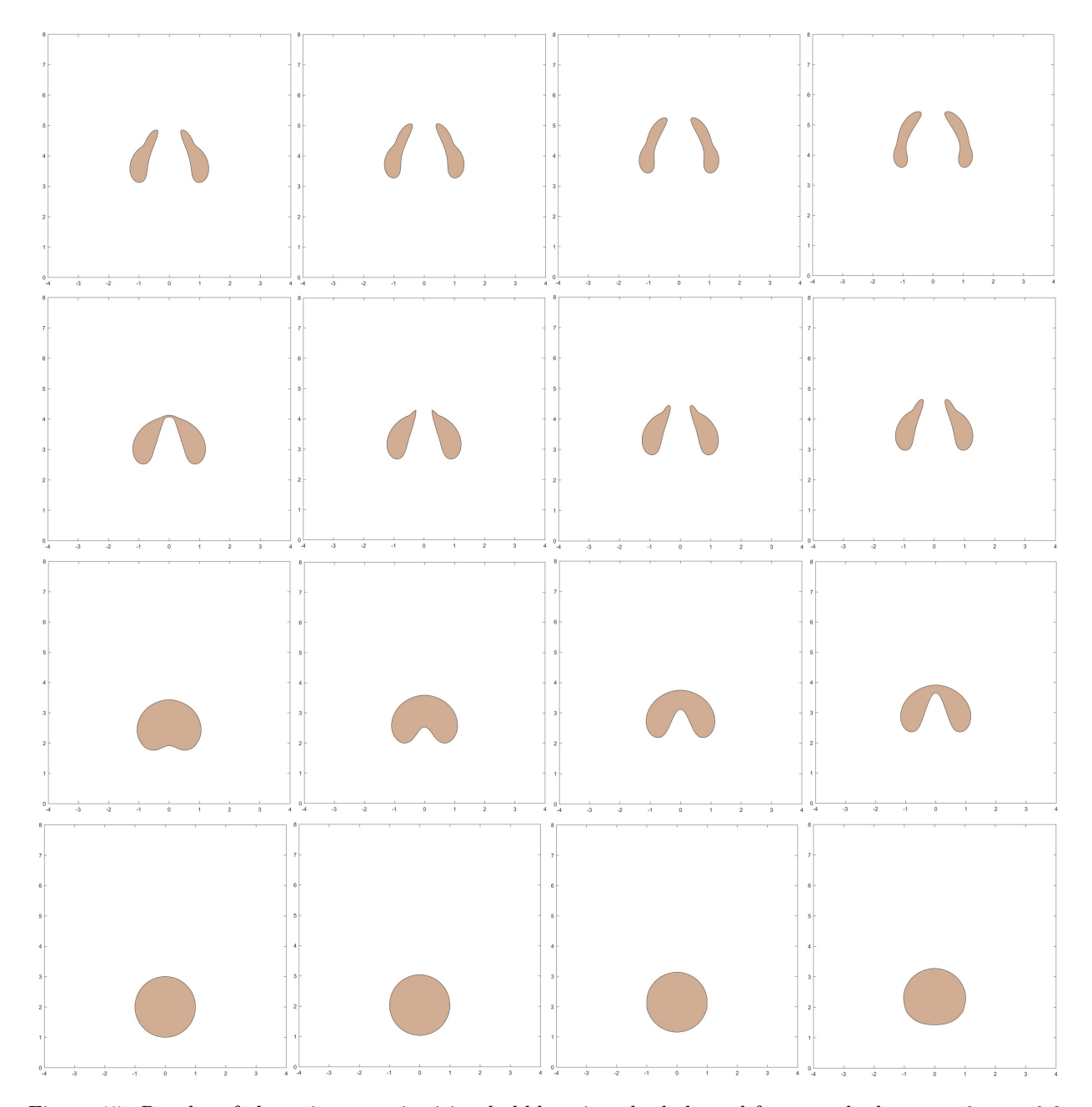


Figure 15: Results of the axisymmetric rising bubble using the balanced-force method at t = 0, t = 0.2, t = 0.4,..., t = 3increment, from left to right and from bottom to top.

going to show that our consistent formulation can be straightforwardly applied to this case.

Considering that there are N phases and that each phase has its own order parameter ϕ_k , the conservative vector-valued Allen-Cahn equation reads

$$\frac{\partial \phi_k}{\partial t} + \nabla \cdot (\mathbf{u}\phi_k) = M\lambda \left(\nabla^2 \phi_k - \frac{1}{\eta^2} g'(\phi_k) + \frac{1}{\eta^2} \alpha \frac{1 + \phi_k}{2} \right) + W_q q_k(t), \tag{62}$$

where the Lagrange multiplier α is to enforce the constraint $\sum_{k=1}^{N} \frac{1+\phi_k}{2} = 1$, and the Lagrange multiplier

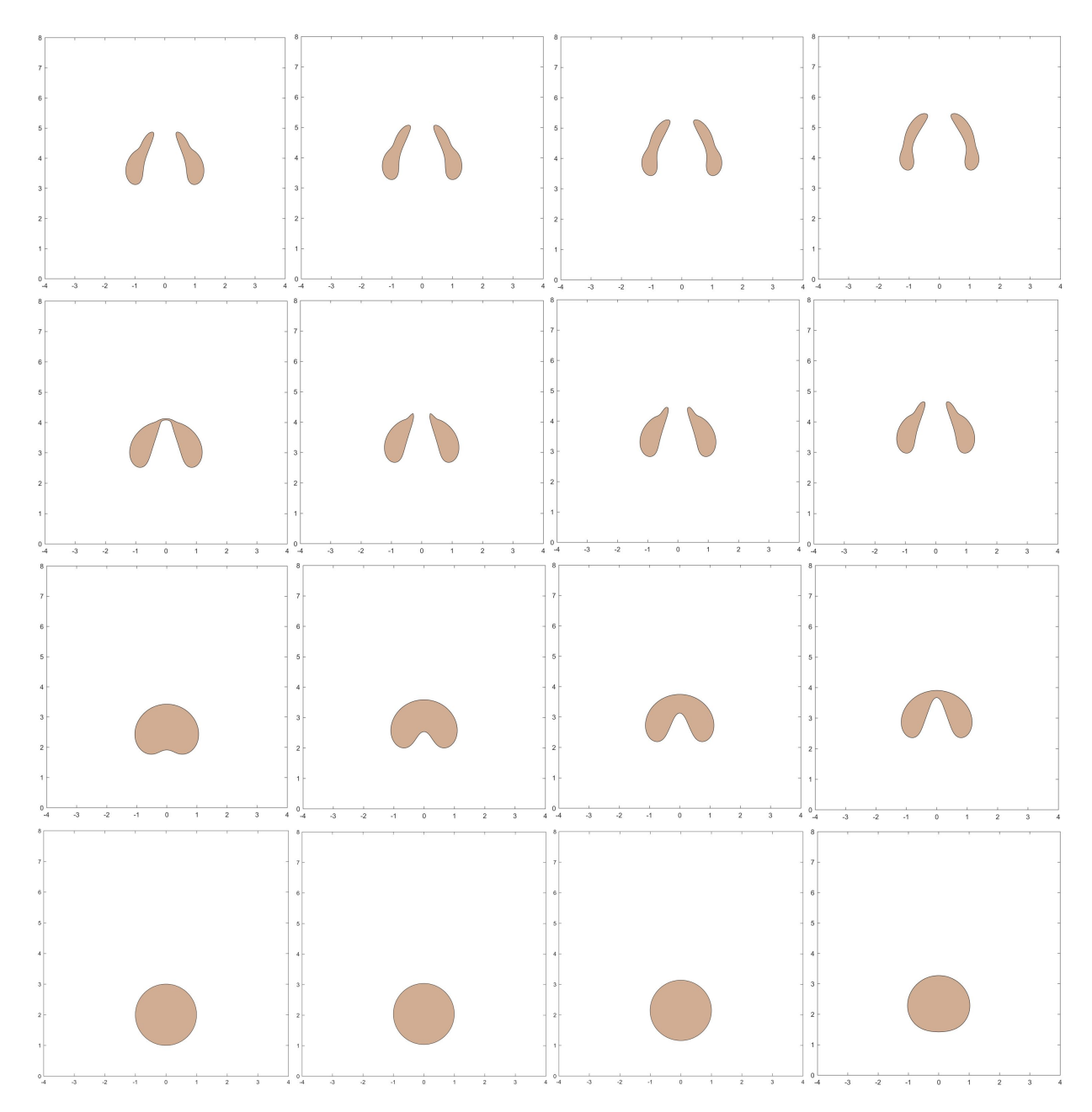


Figure 16: Results of the axisymmetric rising bubble using the conservative method from t = 0 to t = 3 with 0.2 increment, from left to right and from bottom to top.

 $q_k(t)$ is to enforce the constraint $\frac{d}{dt}\int_{\Omega}\phi_k d\Omega=0$ for all k. As a result, α and $q_k(t)$ are

$$\alpha = \sum_{k=1}^{N} g'(\phi_k),\tag{63}$$

and

$$q_k(t) = \frac{\int_{\Omega} \frac{M\lambda}{\eta^2} \left(g'(\phi_k) - \alpha \frac{1+\phi_k}{2} \right) d\Omega}{\int_{\Omega} W_q d\Omega},$$
(64)

where

$$W_q = \sum_{k=1}^{N} 2\sqrt{g(\phi_k)} = \sum_{k=1}^{N} (1 - \phi_k^2). \tag{65}$$

The consistent formulation in Section 2.3 can be directly applied by defining a set of auxiliary variables $\{Q_k\}_{k=1}^N$ that satisfy

$$\nabla \cdot (W_{Q_k} \nabla Q_k) = -\frac{M\lambda}{\eta^2} \left(g'(\phi_k) - \alpha \frac{1 + \phi_k}{2} \right) + W_q q_k(t), 1 \leqslant k \leqslant N, \tag{66}$$

where W_{Q_k} can be chosen as $W_{Q_k} = 2\sqrt{g(\phi_k)} = (1 - \phi_k^2)$. Along with $\mathbf{n} \cdot \nabla Q_k = 0$ at the boundary, Eq.(66) is solvable by considering that

$$0 = \int_{\partial\Omega} W_{Q_k} \mathbf{n} \cdot \nabla Q_k d\Gamma = \int_{\Omega} \nabla \cdot (W_{Q_k} \nabla Q_k) d\Omega = -\int_{\Omega} \frac{M\lambda}{\eta^2} \left(g'(\phi_k) - \alpha \frac{1 + \phi_k}{2} \right) d\Omega + q_k(t) \int_{\Omega} W_q d\Omega = 0.$$
 (67)

As a result, the Phase-Field flux is

$$\mathbf{m}_{\phi_k} = \mathbf{u}\phi_k - M\lambda\nabla\phi_k - W_{Q_k}\nabla Q_k,\tag{68}$$

and the consistent mass flux is

$$\mathbf{m} = \sum_{k=1}^{N} \frac{\rho_k}{2} (\mathbf{u} + \mathbf{m}_{\phi_k}). \tag{69}$$

It can be easily shown that

$$\frac{\partial \rho}{\partial t} + \nabla \cdot \mathbf{m} = \frac{\partial}{\partial t} \sum_{k=1}^{N} \rho_k \frac{1 + \phi_k}{2} + \nabla \cdot \sum_{k=1}^{N} \frac{\rho_k}{2} (\mathbf{u} + \mathbf{m}_{\phi_k}) = \sum_{k=1}^{N} \frac{\rho_k}{2} (\frac{\partial \phi_k}{\partial t} + \nabla \cdot \mathbf{m}_{\phi_k}) = 0.$$
 (70)

Thus, the mass flux defined in Eq.(69) satisfies the *consistency of mass conservation*, i.e., Eq.(70), and should be applied to the inertial term of the momentum equation.

With some minor modifications, the scheme for the conservative Allen-Cahn equation in Section 3.1 can be applied to the conservative vector-valued Allen-Cahn equation Eq.(62). Step 1 is the same as Eq.(25). In Step 2, the two Lagrange multipliers α^* and q_k^* are computed as

$$\alpha^* = \sum_{k=1}^{N} \left(\tilde{g}'(\phi_k^*) - \eta^2 \tilde{\nabla} \cdot \tilde{\nabla} \phi_k^* \right) \tag{71}$$

and

$$q_k^* = \frac{\sum_{i,j} \left[\frac{M\lambda}{\eta^2} \left(\tilde{g}'(\phi_k^*) - \alpha^* \frac{1 + \phi_k^n}{2} \right) \Delta \Omega \right]_{i,j}}{\sum_{i,j} [W_q^n \Delta \Omega]_{i,j}}.$$
 (72)

Finally, in Step 3, ϕ_k^{n+1} is updated as

$$\frac{\gamma_t \phi_k^{n+1} - \gamma_t \phi_k^*}{\Delta t} = \frac{M\lambda}{\eta^2} \alpha^* \frac{1 + \phi_k^n}{2} + W_q^n q_k^*. \tag{73}$$

It can be easily shown that the scheme honors the conservation constraint, i.e., $\sum_{i,j} [\phi_k^{n+1} \Delta \Omega]_{i,j} = \sum_{i,j} [\phi_k^0 \Delta \Omega]_{i,j}$. To satisfy the summation of the volume fractions to be unity, i.e., $\sum_{k=1}^{N} \frac{1+\phi_k^{n+1}}{2} = 1$, the convection scheme proposed in [23] for multiphase incompressible flows should be used.

An example of three-phase Rayleigh-Taylor instability is presented here, where an additional phase is placed on the top, whose density is 4.5. We name the fluids Phases 1, 2, and 3 from the top to bottom, and

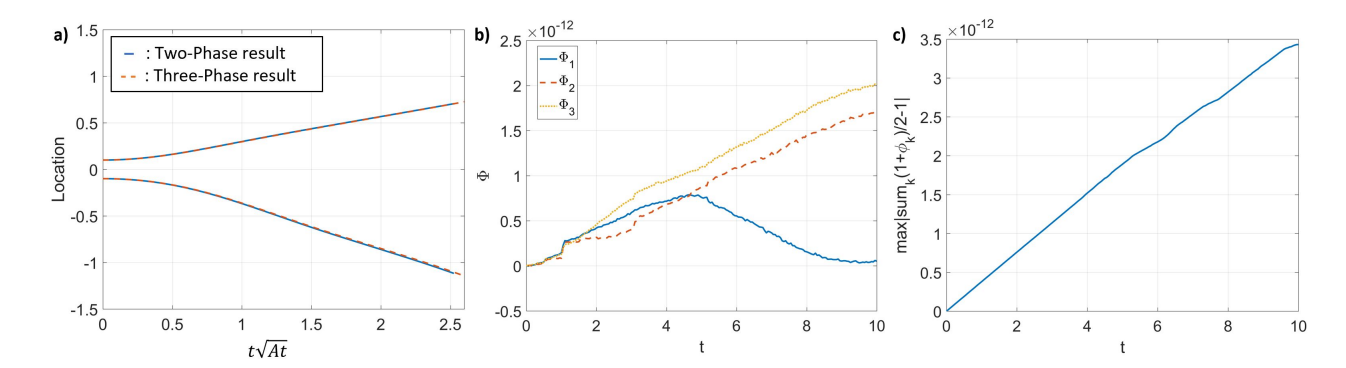


Figure 17: Results of the three-phase Rayleigh-Taylor instability. a) The locations of the interface between Phases 2 and 3 at the center and the lateral edge of the domain, b) $(\Phi_k - \Phi_k|_{t=0})$ versus t, c) max $|\sum_k \frac{1+\phi_k}{2}-1|$ versus t.

we have two Atwood numbers, which are $At_{1,2} = 0.2$ and $At_{2,3} = 0.5$. As a result, the total height of the domain is 6. We use 64×384 cells and the time step is $\Delta t = 10^{-3}$. The rest of the set up is the same as those in Section 4.2.1. The result is shown in Fig.17. Since the two interfaces are far separated, the initial dynamics of Phases 2 and 3, whose Atwood number is 0.5, should be the same as the one in Section 4.2.1 (see Fig.17 a)). Fig.17 b) and c) show that the scheme satisfies the conservation constraint and the summation of the volume fractions is unity everywhere. The evolution of the interfaces is shown in Fig.18, where the complicated interactions among the three phases are observed.

5.2 Application to the improved Cahn-Hilliard model

Some recent studies have focused on improving the Cahn-Hilliard model for incompressible two-phase flows. One common way to do that is to include a flux corresponding to the interfacial profile correction [40, 79, 78]. Since the equation is written in a conservative form, the consistency analysis can be directly applied, which has been discussed in [22]. Another way is to add some Lagrange multipliers to enforce the constraints. As a result, the equation is not in a conservative form, which casts challenges on satisfying the consistency conditions. Thanks to the consistent formulation proposed in the present work, we can reformulate the equation in a conservative form, after which the consistency analysis can be performed. As an example, we consider the improved Cahn-Hilliard model recently proposed by Hu et al.[21], and it reads

$$\frac{\partial \phi}{\partial t} + \nabla \cdot (\mathbf{u}\phi) = \nabla \cdot (M\nabla \xi) + S[\gamma_1(t), \gamma_2(t)],\tag{74}$$

where the newly added term $S[\gamma_1(t), \gamma_2(t)]$ is the Lagrange multiplier to enforce the conservation of total mass, i.e., $\frac{d}{dt} \int_{\Omega} \phi d\Omega = 0$, and the conservation of the mass enclosed by the interface, i.e., $\frac{d}{dt} \int_{\Omega} H(\phi) d\Omega = 0$, with $H(\phi)$ the Heaviside function. We refer interested readers to [21] for the definition of $S[\gamma_1(t), \gamma_2(t)]$. After applying the consistent formulation to $S[\gamma_1(t), \gamma_2(t)]$, and we obtain

$$S[\gamma_1(t), \gamma_2(t)] = \nabla \cdot (W_Q(\phi)\nabla Q). \tag{75}$$

The global mass conservation implies that $\int_{\Omega} S[\gamma_1(t), \gamma_2(t)] d\Omega = 0$ from Eq.(74). When we integrate Eq.(75) in the domain of interest, along with the periodic or homogeneous Neumann boundary condition for Q, both sides of Eq.(75) are zeros. Thus, Eq.(75) is solvable. Consequently, Eq.(74) is reformulated into a conservative form, after which the consistency analyses can be performed. The Phase-Field flux becomes

$$\mathbf{m}_{\phi} = \mathbf{u}\phi - M\nabla\xi - W_{O}(\phi)\nabla Q,\tag{76}$$

and the consistent mass flux is defined the same as Eq.(18). A consistent scheme can be developed, following the procedures in [22] for the Cahn-Hilliard model.

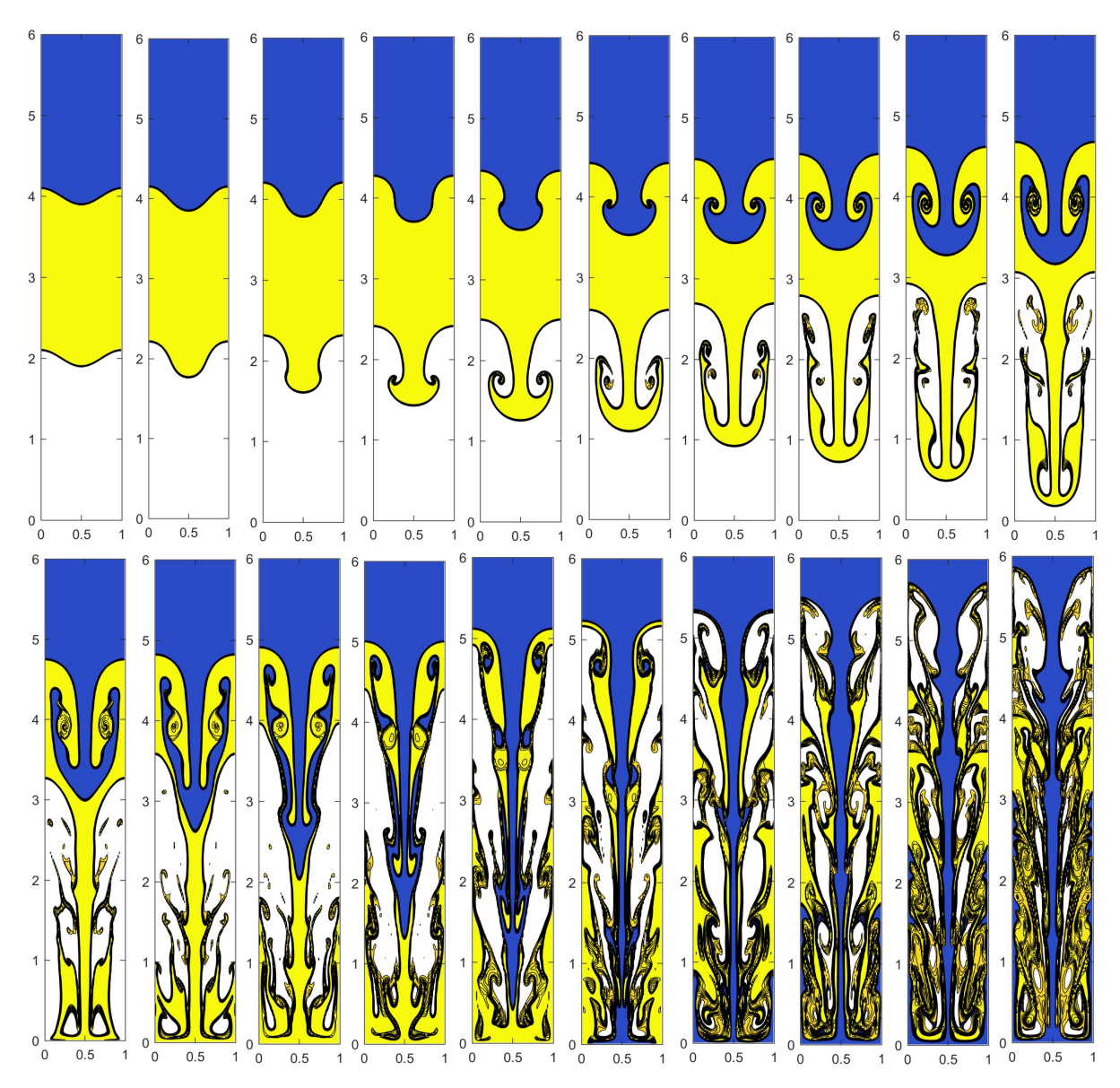


Figure 18: Evolution of the interfaces in the three-phase Rayleigh-Taylor instability problem at t = 0, t = 1, t = 1.5, t = 2,..., t = 10, from left to right and from top to bottom.

5.3 Maximum principle in the discrete level

In section 3.6, we proposed a consistent and conservative boundedness mapping algorithm to enforce the maximum principle in the discrete level. An alternative way is to design a scheme that satisfies the maximum principle directly. Weng and Zhuang [68] proposed an operator splitting scheme along with the Fourier spectral method to solve the conservative Allen-Cahn equation without convection. They show that their scheme satisfies the maximum principle, while it does not conserve mass exactly. Joshi and Jaiman [32, 31] introduced the positivity preserving stabilization term to the variational form of the conservative Allen-Cahn equation in order to enforce the maximum principle with the finite element method (FEM). Shen et al. [60] proposed a maximum-principle-preserving finite difference scheme for the Allen-Cahn equation with convection and variable mobility while without the Lagrange multiplier to enforce mass conservation. In the following, we propose a 1st-order scheme that preserves both the maximum principle and mass conservation. We use $\|\cdot\|_{\infty}$ to denote the standard infinity norm of a function, a matrix, or a vector.

Lemma 5.1. Let $B = (b_{rs}) \in \mathbb{R}^{N \times N}$ and A = aI - B, where a is a positive constant and I is the identity matrix. If B is a negative diagonally dominant (NDD) matrix, i.e.,

$$b_{rr} \leqslant 0, b_{rr} + \sum_{s \neq r} |b_{rs}| \leqslant 0, \forall r, \tag{77}$$

then A is invertible and its inverse satisfies

$$||A^{-1}||_{\infty} \le \frac{1}{a}.$$
 (78)

The proof of **Lemma** 5.1 is available in [60].

Lemma 5.2. Let $f(\phi)$ to be

$$f(\phi) = \phi - \frac{M\lambda\Delta t}{\eta^2}g'(\phi) + \frac{M\lambda\Delta t}{\eta^2} \frac{W_q(\phi)}{\sum_{i,j} [W_q(\phi)\Delta\Omega]_{i,j}} \sum_{i,j} [g'(\phi)\Delta\Omega]_{i,j},$$
(79)

where $g(\phi)$ and $W_q(\phi)$ are defined by Eq(3) and Eq.(6), respectively. If

$$\phi \in [-1, 1], \frac{M\lambda \Delta t}{\eta^2} \leqslant \frac{1}{4},\tag{80}$$

then

$$||f(\phi)||_{\infty} \leqslant 1. \tag{81}$$

Proof. We first show that the summation term $\frac{\sum_{i,j}[g'(\phi)\Delta\Omega]_{i,j}}{\sum_{i,j}[W_q(\phi)\Delta\Omega]_{i,j}}$ is bounded.

$$\left| \frac{\sum_{i,j} [g'(\phi)\Delta\Omega]_{i,j}}{\sum_{i,j} [W_q(\phi)\Delta\Omega]_{i,j}} \right| = \left| \frac{\sum_{i,j} [\phi(\phi^2 - 1)\Delta\Omega]_{i,j}}{\sum_{i,j} [(1 - \phi^2)\Delta\Omega]_{i,j}} \right| \le \frac{\sum_{i,j} [|\phi|(1 - \phi^2)\Delta\Omega]_{i,j}}{\sum_{i,j} [(1 - \phi^2)\Delta\Omega]_{i,j}} \le \frac{\sum_{i,j} [(1 - \phi^2)\Delta\Omega]_{i,j}}{\sum_{i,j} [(1 - \phi^2)\Delta\Omega]_{i,j}} = 1. \quad (82)$$

As a result, $f(\phi)$ is bounded by $f_+(\phi)$ and $f_-(\phi)$, i.e., $f_-(\phi) \leqslant f(\phi) \leqslant f_+(\phi)$, where

$$f_{\pm}(\phi) = \phi - \frac{M\lambda\Delta t}{\eta^2}g'(\phi) \pm \frac{M\lambda\Delta t}{\eta^2}W_q(\phi) = \phi + \frac{M\lambda\Delta t}{\eta^2}(1 - \phi^2)(\phi \pm 1). \tag{83}$$

Notice that $f_{\pm}(\pm 1) = \pm 1$, so if f_{\pm} are monotonically increasing functions for $\phi \in [-1, 1]$, then $-1 \leqslant f_{-}(\phi) \leqslant f(\phi) \leqslant f_{+}(\phi) \leqslant 1$, or equivalently $||f(\phi)||_{\infty} \leqslant 1$. The derivative of $f_{+}(\phi)$ is

$$f'_{+}(\phi) = 1 - 3\frac{M\lambda\Delta t}{\eta^2} \left((\phi + \frac{1}{3})^2 - \frac{4}{9} \right),$$
 (84)

and its minimum for $\phi \in [-1, 1]$ is $\left(1 - \frac{4M\lambda \Delta t}{\eta^2}\right)$ at $\phi = 1$. With a similar procedure, the minimum of $f'_{-}(\phi)$ for $\phi \in [-1, 1]$ is $\left(1 - \frac{4M\lambda \Delta t}{\eta^2}\right)$ at $\phi = -1$. Thus $f_{\pm}(\phi)$ are monotonic increasing when $\frac{M\lambda \Delta t}{\eta^2} \leqslant \frac{1}{4}$. As a result, $||f(\phi)||_{\infty} \leqslant 1$.

The maximum-principle-preserving and conservative scheme for the conservative Allen-Cahn equation reads,

$$\phi^{n+1} - \Delta t \left(M \lambda \tilde{\nabla} \cdot \tilde{\nabla} \phi^{n+1} - \tilde{\nabla} \cdot (\mathbf{u}^n \tilde{\phi}^{n+1}) \right) = \phi^n - \frac{M \lambda \Delta t}{\eta^2} g'(\phi^n) + \frac{M \lambda \Delta t}{\eta^2} \frac{W_q(\phi^n)}{\sum_{i,j} [W_q(\phi^n) \Delta \Omega]_{i,j}} \sum_{i,j} [g'(\phi^n) \Delta \Omega]_{i,j},$$

$$(85)$$

where $\tilde{\phi}$ represents the 1st-order upwind scheme. The left-hand side (LHS) of Eq.(85) can be represented as $A\phi^{n+1} = (I-B)\phi^{n+1}$, where B is the discrete Laplace operator minus the 1st-order upwind operator and

is a NDD matrix [60]. The right-hand side (RHS) of Eq.(85) is $f(\phi^n)$, where $f(\phi)$ is defined in **Lemma** 5.2. Given $\|\phi\|_{\infty} \leqslant 1$ up to time level n and $\frac{M\lambda\Delta t}{\eta^2} \leqslant \frac{1}{4}$, $\|\phi^{n+1}\|_{\infty} = \|A^{-1}f(\phi^n)\|_{\infty} \leqslant \|A^{-1}\|_{\infty} \|f(\phi^n)\|_{\infty} \leqslant 1$ with the help of **Lemma** 5.1 and **Lemma** 5.2. Thus, the maximum principle is preserved in the discrete level. When we sum Eq.(85) over all the cells, the remaining term on the left-hand side (LHS) is $\sum_{i,j} [\phi^{n+1}\Delta\Omega]_{i,j}$ and the remaining term on the right-hand side (RHS) is $\sum_{i,j} [\phi^n\Delta\Omega]_{i,j}$. Consequently, $\sum_{i,j} [\phi^{n+1}\Delta\Omega]_{i,j} = \sum_{i,j} [\phi^n\Delta\Omega]_{i,j}$. If the mass is conserved up to time level n, i.e., $\sum_{i,j} [\phi^n\Delta\Omega]_{i,j} = \sum_{i,j} [\phi^0\Delta\Omega]_{i,j}$, then we have $\sum_{i,j} [\phi^{n+1}\Delta\Omega]_{i,j} = \sum_{i,j} [\phi^0\Delta\Omega]_{i,j}$, which implies the mass conservation in the discrete level.

Although the scheme in Eq.(85) preserves the maximum principle and mass conservation, it is only 1st-order accurate. Designing a higher-order scheme that preserves the maximum principle is non-trivial and could be a future direction of study.

6 Conclusions and future works

In the present work, we consider the conservative Allen-Cahn model and applied it to two-phase flows in a consistent and conservative manner. Our major focus is on the model proposed by Brassel and Bretin [7], where the Lagrange multiplier, enforcing the conservation constraint, is effective only in the interfacial region. Three consistency conditions, which are the consistency of reduction, the consistency of mass conservation, and the consistency of mass and momentum transport, proposed by Huang et al. in [22], are implemented. These consistency conditions are important for producing physical solutions of two-phase flow problems. However, the conservation constraint is enforced by a Lagrange multiplier in the conservative Allen-Cahn equation. As a result, the conservative Allen-Cahn equation has a form of convection-diffusion-reaction equation, and is not in a conservative form, although it satisfies the conservation constraint. Consequently, the consistency analysis can not be directly applied. To resolve this issue, we propose a consistent formulation, where the conservative Allen-Cahn equation, whose original form is a convection-diffusion-reaction equation, is reformulated in a conservative form with the help of defining an auxiliary variable. The auxiliary variable is governed by a Poisson equation, whose source term is compatible with its boundary condition. As a result, the consistency analysis is performed on the reformulated equation, and a consistent two-phase model using the conservative Allen-Cahn equation is developed, which is shown to satisfy all the consistency conditions, mass and momentum conservation, and the energy law of the two-phase system.

A consistent and conservative scheme is developed to solve the proposed two-phase model. The scheme is decoupled, semi-implicit, and formally 2nd-order accurate. One can show that the scheme satisfies all the consistency conditions as well as mass conservation in the discrete level. The momentum is conserved in the discrete level when using the conservative method to compute the surface force while it is essentially conserved when using the balanced-force method. The two methods are proposed in [23] for multiphase flows. A consistent and conservative boundedness mapping algorithm is proposed to enforce the maximum principle of the conservative Allen-Cahn model, while the consistency and conservation properties of the scheme are not influenced. The aforementioned properties of the scheme are carefully validated. In addition, the numerical force balance of the scheme is examined and the balanced-force method outperforms in this case. The convergence behavior of the numerical Phase-Field solution to the sharp interface solution is also studied in a case including large density and viscosity ratios, surface tension, and gravity, and the result shows that the convergence rate is between 1.5th to 2nd order. This behavior is also observed in the pure advection tests without hydrodynamics. Our numerical experiments show that the energy law is preserved in the discrete level by the scheme no matter whether the boundedness mapping algorithm is activated. The significance of the consistency conditions on preserving the physical momentum transport is also illustrated. Three realistic two-phase flow problems, which include strong interactions between the fluid phases, a large difference of material properties, and topological changes, are performed. In these applications, we observe that the balanced-force method has a larger tendency to break to small interfacial structures, resulting in more topological changes, while the conservative method is more stable, i.e., accepting a larger time step. The consistent formulation and the proposed scheme can be easily applied in different coordinate systems, e.g., the axisymmetric coordinate, and the axisymmetric rising bubble is performed to show the flexibility of our scheme. In addition, the consistent formulation can be straightforwardly extended to the conservative vector-valued Allen-Cahn equation [34] for multiphase flows, and the proposed scheme can be applied to those problems with some minor modifications. The three-phase Rayleigh-Taylor instability problem is presented as an example. Its application to the improved Cahn-Hilliard model [21] is discussed, and an alternative 1st-order scheme that preserves both the maximum principle and conservation is proposed. In summary, the proposed scheme is accurate, robust, and effective for complicated two-phase flows, and it is flexible and generalized for multiphase problems and for other Phase-Field models.

Although the analyses and numerical results presented in the present work are two-dimensional, the proposed scheme can be readily applied to higher dimensions without changing its properties. However, those computations require efficient parallel programming, which is outside the scope of the present work, and we leave it to future works. Another attractive future direction is to extend the present scheme to the adaptive time and space refinements, which would be especially beneficial for the problems including a wide range of time and length scales. However, preserving the consistent and conservative properties of the scheme can be non-trivial. There are many Phase-Field models that are plausible for two-phase flow problems, while the quantitative comparisons among them are rare. Which Phase-Field model performs best in two-phase flows is still an open question, and the pros and cons of each model are far from clear. Some recent works related to that include the comparisons between different conservative Allen-Cahn models [7, 35], the comparisons among the conservative Allen-Cahn models and the Cahn-Hilliard models [38], the comparisons between the conservative Allen-Cahn model and the conservative Phase-Field model [9], and the comparisons among the Cahn-Hilliard model and its variants [61, 21]. It should be noted that the comparisons in [7, 35, 38, 9] do not include hydrodynamics, while the consistency conditions are not considered in [61, 21] and the major focus in [61] is on the matched density cases. So far, all the Phase-Field models either are written in a conservative form or can be reformulated in a conservative form using our consistent formulation. As a result, the consistency analysis in [22] can be performed. A valuable future work would be a careful comparison among different Phase-Field models for two-phase flows under the consistent and conservative framework and for problems including a large difference in material properties. We believe such studies can shed light on choosing the Phase-Field model appropriate for two-phase problems.

Appendix

Two additional cases, which are the reversed single vortex problem [54] and the Zalesak's disk problem [77], are supplemented to validate the conservative Allen-Cahn model as an interface-capturing method.

Reversed single vortex

We follow the set up in [54]. The domain is $[1 \times 1]$ and a circle with a radius r = 0.15 is initially at $(x_r, y_r) = (0.5, 0.75)$. The velocity is derived from the streamfunction

$$\psi_s = \frac{1}{\pi} \sin^2(\pi x) \sin^2(\pi y) \cos(\frac{\pi t}{T}),\tag{86}$$

where T=2. The cell size h is ranging from $\frac{1}{25}$ to $\frac{1}{200}$ and the time step is determined by the CFL constraint, i.e., CFL = $|u|_{\max}\Delta t/h=0.1$. η and M are set exactly the same as those in Section 4.1.3, i.e., $\eta=\eta_0(h/h_0)$ and $M=M_0(\eta/\eta_0)$, with $\eta_0=h_0=1/32$ and $M_0=10^{-7}$. The maximum deformation happens at t=T/2, after which the flow reverses. At t=T, the interface should return to its initial location and shape. To quantify the performance of the conservative Allen-Cahn model as an interface-capturing method, the L_2 norm, i.e., the root mean square, of Er is computed. Er is defined as

$$Er = r - \sqrt{(x_s - x_r)^2 + (y_s - y_r)^2},$$
(87)

where (x_s, y_s) are the points of the zero contour of the order parameter at t = T, i.e., $\phi(x_s, y_s, T) = 0$.

The results are shown in Fig.19, where the interfaces at t=0, t=T/2, and t=T are plotted. One can observe the convergence of the Phase-Field solution to the exact solution as the cell size is reduced. The L_2 norm of Er is listed in Table 8 and the convergence rate is above 1.5th-order, which is consistent with the results in Section 4.1.3.

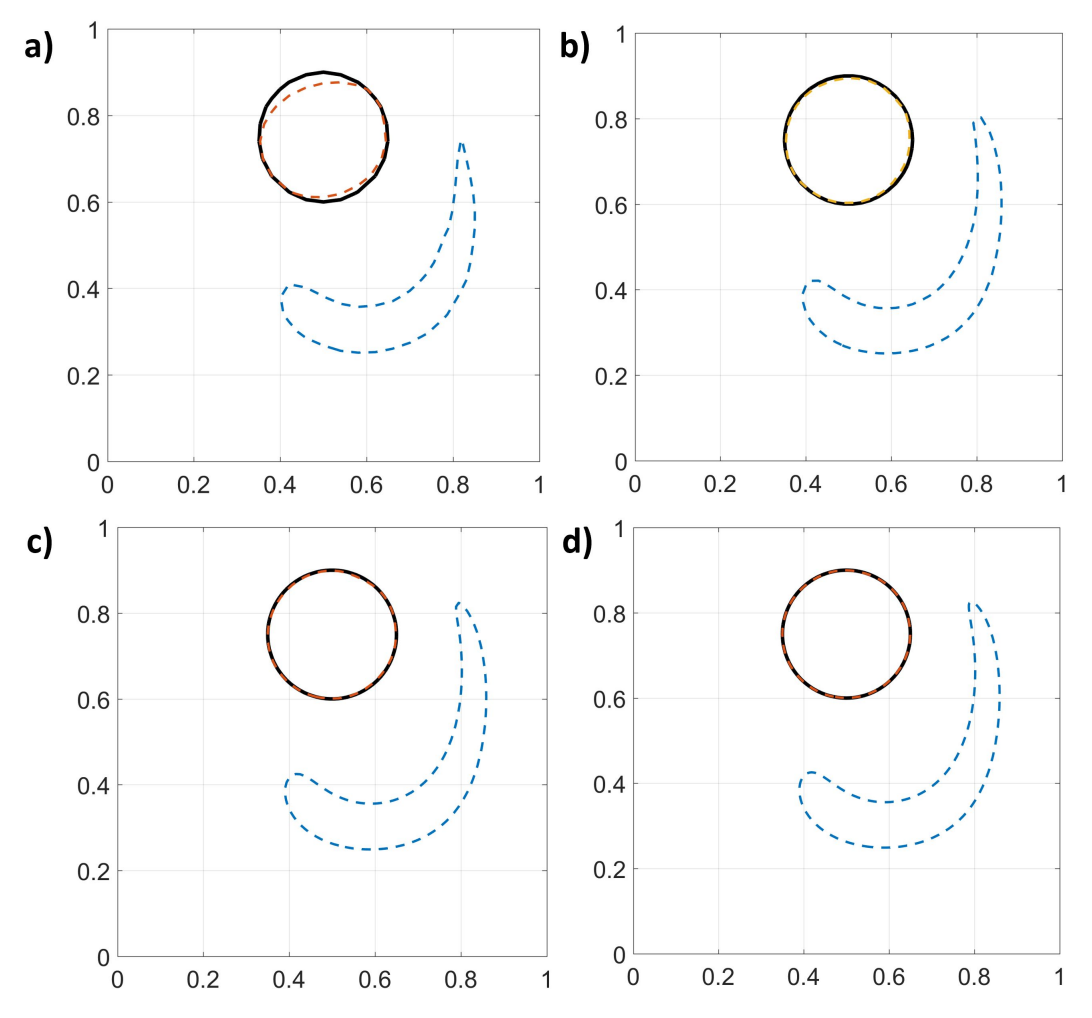


Figure 19: Results of the reversed single vortex problem at t=0 (black solid line), $t=\frac{T}{2}$ (blue dashed line), t=T (red dashed line). a) $h=\frac{1}{25}$, b) $h=\frac{1}{50}$, c) $h=\frac{1}{100}$ and d) $h=\frac{1}{200}$.

Table 8: L_2 error of the reversed single vortex problem

Grid	L_2	order
25	1.32e-2	1.54
50	4.55e-3	1.56
100	1.55e-3	1.73
200	4.67e-4	

Zalesak's disk

The Zalesak's disk problem proposed in [77] is performed. The domain is $[1 \times 1]$ and the velocity is defined from the streamfunction below

$$\psi_s = \frac{1}{2}\Omega_0[(x - x_0)^2 + (y - y_0)^2],\tag{88}$$

where $\Omega_0=1$, $x_0=0.5$ and $y_0=0.5$. The cell size h is ranging from $\frac{1}{25}$ to $\frac{1}{200}$ and the time step is determined from the CFL constraint, i.e., CFL = $\Omega_0 \Delta t/h = 0.1$. η and M are $\eta = \eta_0 (h/h_0)$ and $M = M_0 (\eta/\eta_0)$ with $\eta_0=h_0=1/32$ and $M_0=10^{-7}$, which is the same as those in Section 4.1.3. A circle with a radius r=0.15 is notched by a rectangle whose width is 0.05 and length is 0.2. This notched circle is initially at $(x_r,y_r)=(0.5,0.75)$ and will rotate rigidly around (0.5,0.5). At $t=2\pi$, the notched circle finishes one

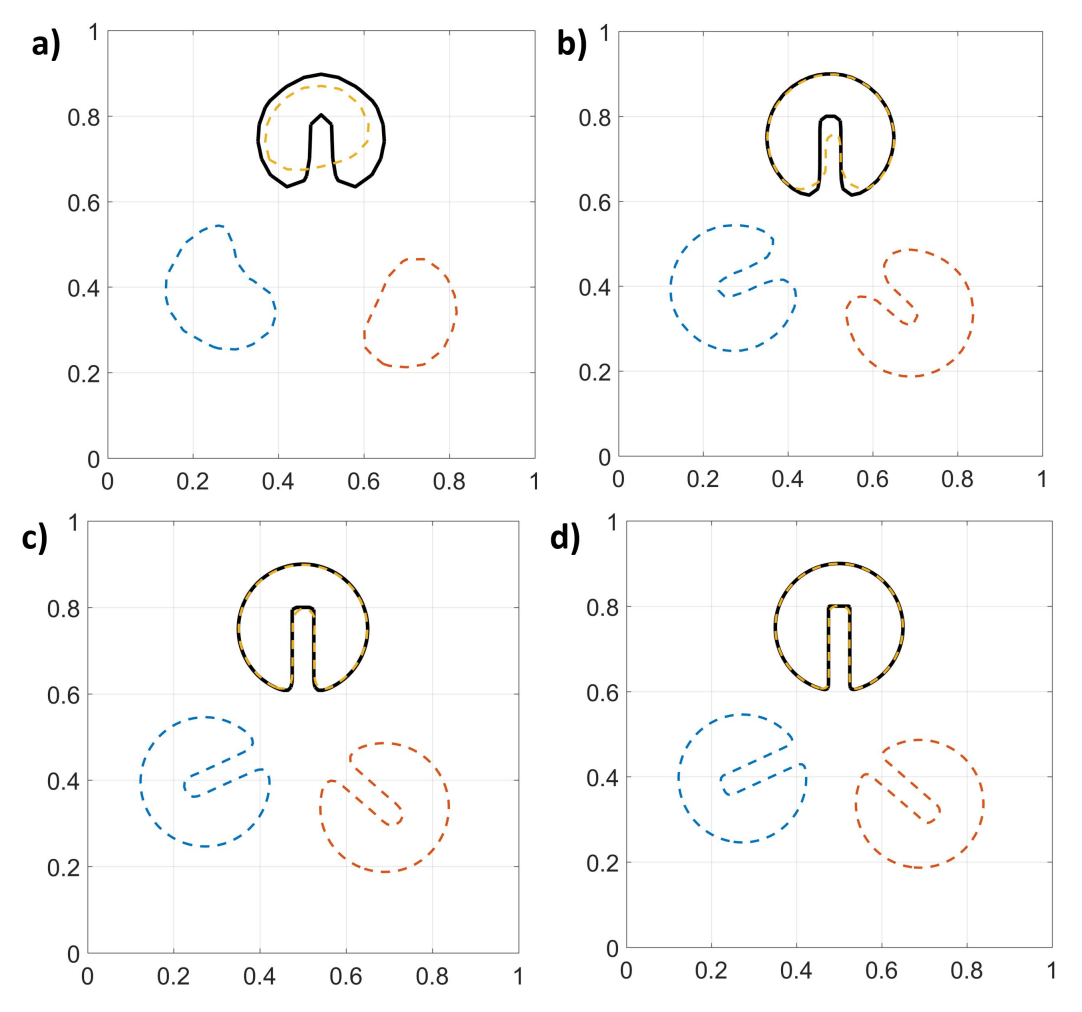


Figure 20: Results of the Zalesak's disk problem at t=0 (black solid line), t=2 (blue dashed line), t=4 (red dashed line), and $t=2\pi$ (yellow dashed line). a) $h=\frac{1}{25}$, b) $h=\frac{1}{50}$, c) $h=\frac{1}{100}$ and d) $h=\frac{1}{200}$.

Table 9: L_2 error of the Zalesak's disk problem

Grid	L_2	order
25	8.17e-2	1.37
50	3.16e-2	1.87
100	8.64e-3	2.86
200	1.19e-3	

period of rotation and should return to its initial position. To evaluate the performance of the conservative Allen-Cahn model as an interface-capturing method, the L_2 norm of Er is used. Er is defined as

$$Er = \sqrt{[x_I(s; t=2\pi) - x_I(s; t=0)]^2 + [y_I(s; t=2\pi) - y_I(s; t=0)]^2},$$
(89)

where $x_I(s;t)$ and $y_I(s;t)$ are the cubic spline interpolants using the points (x_s,y_s) at time t satisfying $\phi(x_s,y_s,t)=0$.

Fig.20 shows the interfaces at t = 0, t = 2, t = 4, and $t = 2\pi$. The convergence of the Phase-Field solution to the exact solution with grid refinement is obvious. The L_2 norm of Er is listed in Table 9. The convergence rate is fast, and this can be attributed to the rigid body motion of the problem.

Acknowledgments

A.M. Ardekani would like to acknowledge the financial support from National Science Foundation (CBET-1705371). This work used the Extreme Science and Engineering Discovery Environment (XSEDE) [64], which is supported by the National Science Foundation grant number ACI-1548562 through allocation TG-CTS180066 and TG-CTS190041. G. Lin would like to acknowledge the support from National Science Foundation (DMS-1555072 and DMS-1736364).

References

- [1] H. Abels, H. Garcke, and G. Grun. Thermodynamically consistent, frame indifferent diffuse interface models for incompressible two-phase flows with different densities. *Mathematical Models and Methods in Applied Sciences*, 22:1150013, 2012.
- [2] M. Alfaro and P. Alifrangis. Convergence of a mass conserving allen—cahn equation whose lagrange multiplier is nonlocal and local. *Interfaces Free Bound.*, 16:243–268, 2014.
- [3] S.M. Allen and J.W. Cahn. A microscopic theory for antiphase boundary motion and its application to antiphase domain coarsening. *Acta Metallurgica*, 27:1085–1095, 1979.
- [4] D.M. Anderson, G.B. McFadden, and A.A. Wheeler. Diffuse-interface methods in fluid mechanics. *Annu. Rev. Fluid Mech.*, 30:139–165, 1998.
- [5] F. Boyer and C. Lapuerta. Study of a three component cahn-hilliard flow model. ESAIM: Mathematical Modelling and Numerical Analysis, 40(4):653–687, 2006.
- [6] J.U. Brackbill, D.B. Kothe, and C. Zemach. A continuum method for modeling surface tension. J. Comput. Phys., 100:335–354, 1992.
- [7] M. Brassel and E. Bretin. A modified phase field approximation for mean curvature flow with conservation of the volume. *Math Method Appl. Sci.*, 10:1157–1180, 2011.
- [8] J.W. Cahn and J.E. Hilliard. Free energy of a nonuniform system, i interfacial free energy. J. Chem. Phys., 28:258-267, 1958.
- [9] Z. Chai, D. Sun, H. Wang, and B. Shi. A comparative study of local and nonlocal allen-cahn equations with mass conservation. *J. Fluid Mech.*, 122:631–642, 2018.
- [10] X. Chen, D. Hilhorst, and E. Logak. Mass conserving allen-cahn equation and volume preserving mean curvature flow. *Interfaces and Free Boundaries*, 12:527–549, 2010.
- [11] R. Chiodi and O. Desjardins. A reformulation of the conservative level set reinitialization equation for accurate and robust simulation of complex multiphase flows. J. Comput. Phys., 343:186–200, 2017.
- [12] P-H Chui and Y-T Lin. A conservative phase-field method for solving incompressible two-phase flows. J. Comput. Phys., 230:185–204, 2011.
- [13] H. Ding, P.D.M. Spelt, and C. Shu. Diffuse interface model for incompressible two-phase flows with large density ratios. *J. Comput. Phys.*, 226:2078–2095, 2007.
- [14] S. Dong. Multiphase flows of n immiscible incompressible fluids: A reduction-consistent and thermodynamically-consistent formulation and associated algorithm. *J. Comput. Phys.*, 361:1–49, 2018.
- [15] S. Dong and J. Shen. A time-stepping scheme involving constant coefficient matrices for phase-field simulations of two-phase incompressible flows with large density ratios. J. Comput. Phys., 231:5788–5804, 2012.
- [16] R.P. Fedkiw, T. Aslam, B. Merriman, and S. Osher. A non-oscillatory eulerian approach to interfaces in multimaterial flows (the ghost fluid method). *J. Comput. Phys.*, 152:457–492, 1999.

- [17] M.M. Francois, J.S. Cummins, E.D. Dendy, D.B. Kothe, M.J. Sicilian, and W.W. Williams. A balanced-force algorithm for continuous and sharp interfacial surface tension models within a volume tracking framework. J. Comput. Phys., 213:141–173, 2006.
- [18] F. Gibou, R. Fedkiw, and S. Osher. A review of level-set methods and some recent applications. *J. Comput. Phys.*, 353:82–109, 2018.
- [19] J.L. Guermond and L. Quartapelle. A projection fem for variable density incompressible flows. J. Comput. Phys., 165:167–188, 2000.
- [20] C.W. Hirt and B.D. Nichols. Volume of fluid (vof) method for the dynamics of free boundaries. *J. Comput. Phys.*, 39:201–225, 1981.
- [21] Y. Hu, Q. He, D. Li, Y. Li, and X. Niu. On the total mass conservation and the volume preservation in the diffuse interface method. *Comput. Fluids*, 193:104291, 2019.
- [22] Z. Huang, G. Lin, and A.M. Ardekani. Consistent, essentially conservative and balanced-force phase-field method to model incompressible two-phase flows. *J. Comput. Phys.*, pages 109192, doi: https://doi.org/10.1016/j.jcp.2019.109192., 2020.
- [23] Z. Huang, G. Lin, and A.M. Ardekani. A consistent and conservative phase-field method for multiphase incompressible flows. Submitted.
- [24] S. Hysing, S. Turek, D. Kuzmin, N. Parolini, E. Burman, S. Ganesan, and L. Tobiska. Quantitative benchmark computations of two-dimensional bubble dynamics. *Int. J. Numer. Methods. Fluids*, 60:1259– 1288, 2009.
- [25] Satoshi Ii, Kazuyasu Sugiyama, Shintaro Takeuchi, Shu Takagi, Yoichiro Matsumoto, and Feng Xiao. An interface capturing method with a continuous function: The thinc method with multi-dimensional reconstruction. *J. Comput. Phys.*, 231(5):2328–2358, 2012.
- [26] D. Jacqmin. Calculation of two-phase navier-stokes flows using phase-field modeling. J. Comput. Phys., 155:96–127, 1999.
- [27] D. Jacqmin. Contact-line dynamics of a diffuse fluid interface. J. Fluid Mech., 402:57–88, 2000.
- [28] D. Jamet, D. Torres, and J.U. Brackbill. On the theory and computation of surface tension: The elimination of parasitic currents through energy conservation in the second-gradient method. *J. Comput. Phys.*, 182:262–276, 2002.
- [29] D. Jeong and J. Kim. Conservative allen-cahn-navier-stokes system for incompressible two-phase fluid flows. Comput. Fluids, 156:239–246, 2017.
- [30] G-S Jiang and C-W Shu. Efficient implementation of weighted eno schemes. *J. Comput. Phys.*, 126:202–228, 1996.
- [31] V. Joshi and R.K. Jaiman. An adaptive variational procedure for the conservative and positivity preserving allen–cahn phase-field model. *J. Comput. Phys.*, 336:478–504, 2018.
- [32] V. Joshi and R.K. Jaiman. A positivity preserving and conservative variational scheme for phase-field modeling of two-phase flows. *J. Comput. Phys.*, 360:137–166, 2018.
- [33] J. Kim. Phase-field models for multi-component fluid flows. Commun. Comput. Phys., 12:613–661, 2012.
- [34] J. Kim and H.G. Lee. A new conservative vector-valued allen-cahn equation and its fast numerical method. Comput. Phys. Commun., 221:102–108, 2017.
- [35] J. Kim, S. Lee, and Y. Choi. A conservative allen–cahn equation with a space–time dependent lagrange multiplier. *Int. J. Eng. Sci.*, 84:11–17, 2014.

- [36] B. Lalanne, L.R. Villegas, S. Tanguy, and F. Risso. On the computation of viscous terms for incompressible two-phase flows with level set/ghost fluid method. *J. Comput. Phys.*, 301:289–307, 2015.
- [37] L. Leal. Advanced Transport Phenomena: Fluid Mechanics and Convective Transport Processes. Cambridge University Press, 2007.
- [38] D. Lee and J. Kim. Comparison study of the conservative allen–cahn and the cahn–hilliard equations. *Math. Comput. Simulation*, 119:35–56, 2016.
- [39] H.G. Lee. High-order and mass conservative methods for the conservative allen–cahn equation. *Comput. Math. Appl.*, 72:620–631, 2016.
- [40] Y. Li, J.I. Choi, and J. Kim. A phase-field fluid modeling and computation with interfacial profile correction term. Commun. Nonlinear Sci. Numer. Simulat., 30:84–100, 2016.
- [41] C. Liu, J. Shen, and X. Yang. Decoupled energy stable schemes for a phase-field model of two-phase incompressible flows with variable density. *J Sci Comput*, 62:601–622, 2015.
- [42] F. Magaletti, F. Picano, M. Chinappi, L. Marino, and C.M. Casciola. The sharp-interface limit of the cahn-hilliard/navier-stokes model for binary fluids. *J. Fluid Mech.*, 714:95–126, 2013.
- [43] J.C. Martin and W.J. Moyce. An experimental study of the collapse of liquid columns on a rigid horizontal plane. Philosophical Transactions of the Royal Society of London, Series A, 244:312–324, 1952.
- [44] S. Mirjalili, C.B. Ivey, and A. Mani. Comparison between the diffuse interface and volume of fluid methods for simulating two-phase flows. *Int. J. Multiph. Flow*, 116:221–238, 2019.
- [45] R.H. Nochetto, A.J. Salgado, and I. Tomas. A diffuse interface model for two-phase ferrofluid flows. Comput. Methods Appl. Mech. Engrg., 309:497–531, 2016.
- [46] E. Olsson and G. Kreiss. A conservative level set method for two phase flow. *J. Comput. Phys.*, 210:225–246, 2005.
- [47] E. Olsson, G. Kreiss, and S. Zahedi. A conservative level set method for two phase flow ii. *J. Comput. Phys.*, 225:785–807, 2007.
- [48] S. Osher and A.J. Sethian. Fronts propagating with curvature-dependent speed: Algorithms based on hamilton-jacobi formulations. *J. Comput. Phys.*, 79:12–49, 1988.
- [49] M. Owkes and O. Desjardins. A mass and momentum conserving unsplit semi-lagrangian framework for simulating multiphase flows. *J. Comput. Phys.*, 332:21–46, 2017.
- [50] S. Popinet. An accurate adaptive solver for surface-tension-driven interfacial flows. *J. Comput. Phys.*, 228:5838–5866, 2009.
- [51] S. Popinet. Numerical models for surface tension. Annu. Rev. Fluid Mech., 50:49-75, 2018.
- [52] L. Qian, Y. Wei, and F. Xiao. Coupled thinc and level set method: A conservative interface capturing scheme with high-order surface representations. *J. Comput. Phys.*, 373:284–303, 2018.
- [53] T. Qian, X.P. Wang, and P. Sheng. A variational approach to moving contact line hydrodynamics. *J. Fluid Mech.*, 564:333–360, 2006.
- [54] W.J. Rider and D.B. Kothe. Reconstructing volume tracking. J. Comput. Phys., 141:112–152, 1998.
- [55] R. Scardovelli and S. Zaleski. Direct numerical simulation of free-surface and interfacial flow. Annu. Rev. Fluid Mech., 31:567–603, 1999.
- [56] J.A. Sethian and P. Smereka. Level set method for fluid interfaces. Annu. Rev. Fluid Mech., 35:341–372, 2003.

- [57] J Shen. Modeling and numerical approximation of two-phase incompressible flows by a phase-field approach. *Multiscale Modeling and Analysis for Materials Simulation*, 22:147–195, 2011.
- [58] J. Shen and X. Yang. Decoupled, energy stable schemes for phase-field models of two-phase incompressible flows. SIAM J. NUMER. ANAL, 53:279–296, 2015.
- [59] J. Shen, X. Yang, and H. Yu. Efficient energy stable numerical schemes for a phase field moving contact line model. *J. Comput. Phys.*, 284:617–630, 2015.
- [60] Jie Shen, Tao Tang, and Jiang Yang. On the maximum principle preserving schemes for the generalized allen–cahn equation. *Commun. Math. Sci.*, 14:1517–1534, 2016.
- [61] G. Soligo, A. Roccon, and A. Soldati. Mass-conservation-improved phase field methods for turbulent multiphase flow simulation. *Acta Mech.*, 230:683–696, 2019.
- [62] M. Sussman and P. Smereka. Axisymmetric free boundary problems. J. Fluid Mech., 341:269–294, 1997.
- [63] M. Sussman, P. Smereka, and S. Osher. A level set approach for computing solutions to incompressible two-phase flow. J. Comput. Phys., 114:146–159, 1994.
- [64] J. Towns, T. Cockerill, M. Dahan, I. Foster, K. Gaither, A. Grimshaw, V. Hazlewood, S. Lathrop, D. Lifka, G.D. Peterson, R. Roskies, J.R. Scott, and N. Wilkins-Diehr. Xsede: accelerating scientific discovery. *Comput. Sci. Eng.*, 16:62–74, 2014.
- [65] G. Tryggvason. Numerical simulations of the rayleigh-taylor instability. J. Comput. Phys., 75:253–282, 1988.
- [66] G. Tryggvason, B. Bunner, A. Esmaeeli, D. Juric, N. Al-Rawahi, W. Tauber, J. Han, S. Nas, and Y.J. Jan. A front-tracking method for the computations of multiphase flow. J. Comput. Phys., 169:708–759, 2001.
- [67] S.O. Unverdi and G. Tryggvason. A front-tracking method for viscous, incompressible, multi-fluid flows. J. Comput. Phys., 100:25–37, 1992.
- [68] Z. Weng and Q. Zhuang. Numerical approximation of the conservative allen–cahn equation by operator splitting method. *Math Method Appl. Sci.*, 40:4462–4480, 2017.
- [69] F Xiao, Y Honma, and T Kono. A simple algebraic interface capturing scheme using hyperbolic tangent function. *Int. J. Numer. Meth. Fluids*, 48(9):1023–1040, 2005.
- [70] B. Xie and F. Xiao. Toward efficient and accurate interface capturing on arbitrary hybrid unstructured grids: The thinc method with quadratic surface representation and gaussian quadrature. J. Comput. Phys., 349:415–440, 2017.
- [71] X. Xu, Y. Di, and H. Yu. Sharp-interface limits of a phase-field model with a generalized navier slip boundary condition for moving contact lines. *J. Fluid Mech.*, 849:805–833, 2018.
- [72] X. Yang, J.J. Feng, C. Liu, and J. Shen. Numerical simulations of jet pinching-off and drop formation using an energetic variational phase-field method. *J. Comput. Phys.*, 218:417–428, 2006.
- [73] P. Yue, J.J. Feng, C. Liu, and J. Shen. A diffuse-interface method for simulating two-phase flows of complex fluids. *J. Fluid Mech.*, 515:293–317, 2004.
- [74] P. Yue, C. Zhou, and J.J. Feng. A computational study of the coalescence between a drop and an interface in newtonian and viscoelastic fluids. *Physics of Fluids*, 18:102102, 2006.
- [75] P. Yue, C. Zhou, and J.J. Feng. Spontaneous shrinkage of drops and mass conservation in phase-field simulations. *J. Comput. Phys.*, 223:1–9, 2007.
- [76] P. Yue, C. Zhou, and J.J. Feng. Sharp-interface limit of the cahn-hilliard model for moving contact lines. J. Fluid Mech., 645:279–294, 2010.

- [77] S.T. Zalesak. Fully multidimensional flux-corrected transport algorithms for fluids. *J. Comput. Phys.*, 31:335–362, 1979.
- [78] T. Zhang, J. Wu, and X. Lin. An interface-compressed diffuse interface method and its application for multiphase flows. *Physics of Fluids*, 31:122102, 2019.
- [79] Y. Zhang and W. Ye. A flux-corrected phase-field method for surface diffusion. *Commun. Comput. Phys.*, 22:422–440, 2017.
- [80] C. Zhou, P. Yue, and J.J. Feng. Dynamic simulation of droplet interaction and self-assembly in a nematic liquid crystal. *Langmuir*, 24:3099–3110, 2008.